

Channel cross-section heterogeneity of particulate organic carbon transport in the Huanghe

Yutian Ke^{1†}, Damien Calmels¹, Julien Bouchez², Marc Massault¹, Benjamin Chetelat³, Aurélie Noret¹, Hongming Cai², Jiubin Chen³, Jérôme Gaillardet², Cécile Quantin¹

¹GEOPS, Université Paris-Saclay-CNRS, 91405 Orsay, France

²Université de Paris, Institut de Physique du Globe de Paris, CNRS, 75005 Paris, France

³School of Earth System Science, Institute of Surface-Earth System Science, Tianjin University, 300072 Tianjin, China

[†]Present address: Division of Geological and Planetary Science, California Institute of Technology, Pasadena, CA 91125, USA

Corresponding author: Yutian Ke (yutianke@caltech.edu)

Abstract. The Huanghe (Yellow River), one of the largest turbid river systems in the world, has long been recognized as a major contributor of suspended particulate matter (SPM) to the ocean. However, over the last few decades, the SPM export flux of the Huanghe has decreased over 90% due to the high management, impacting the global export of particulate organic carbon (POC). To better constrain sources and modes of transport of POC beyond the previously investigated transportation of POC near the channel surface, SPM samples were for the first time collected over a whole channel cross-section in the lower Huanghe. Riverine SPM samples were analyzed for particle size and major element contents, as well as for POC content and dual carbon isotopes (¹³C and ¹⁴C). Clear vertical and lateral heterogeneities of the physical and chemical properties of SPM are observed within the river cross-section. For instance, finer SPM carry in general more POC with higher ¹⁴C activity near the surface of the right bank. Notably, we discuss how bank erosion in the alluvial plain is likely to generate lateral heterogeneity in POC composition. The Huanghe POC is millennial-aged ($4,020 \pm 500$ radiocarbon years), dominated by organic carbon (OC) from the biosphere, while the lithospheric fraction is ca. 12%. The mobilization of aged and refractory OC, including radiocarbon-dead biospheric OC, from deeper soil horizons of the loess-paleosol sequence through erosion in the Chinese Loess Plateau is an important mechanism contributing to fluvial POC in the Huanghe drainage basin. Altogether, anthropogenic activities can drastically change the compositions and transport dynamics of fluvial POC, consequentially altering the feedback of the source-to-sink trajectory of a river system to regional and global carbon cycles.

29 **1 Introduction**

30 Rivers are the main conveyor of rock and soil debris eroded from the continents to the ocean. Along with inorganic
31 material, river sediments host particulate organic carbon (POC) derived mainly from three major sources: 1) recently
32 photosynthesized OC of the biosphere, 2) aged and altered OC from soils, and 3) ancient OC contained in sedimentary
33 rocks (Blair et al., 2010). The net effect of riverine POC transport on the carbon cycle and thus on the evolution of
34 Earth's climate depends on POC provenance and fate. The effective sedimentary burial of POC derived from the
35 terrestrial biosphere (biospheric OC, OC_{bio}) represents a net, long-term sink of atmospheric CO_2 (Galy et al., 2007,
36 Bouchez et al., 2014; Hilton et al., 2015), whereas the oxidation of POC derived from continental rocks (petrogenic
37 OC, OC_{petro}) acts as a net, long-term source of CO_2 to the atmosphere (Hilton et al., 2014). The erosion and burial of
38 OC_{petro} escaping from oxidation has no net effect on the long-term carbon cycle (Galy et al., 2008a; Bouchez et al.,
39 2010; Hilton et al., 2011; Horan et al., 2019). In addition, the reactive nature of OC_{bio} might also result in short-term
40 CO_2 emission during transport from both river channels and recently-deposited sediments (Mayorga et al., 2005; Galy
41 and Eglinton, 2011; Blair and Aller, 2012).

42 Globally, rivers transport a total POC flux of *ca.* 200 Tg C/year, consisting of 157^{+74}_{-50} Tg C/year of OC_{bio} and 43^{+61}_{-25}
43 Tg C/year of OC_{petro} (Galy et al., 2015; Ludwig et al., 1996). Source-to-sink processes controlling the origin and fate
44 of riverine POC are prominently river-specific, suggesting that the impact of POC on regional and global carbon
45 cycles might significantly vary both spatially and temporally (Blair and Aller, 2012). It is thus crucial to understand
46 the mechanisms controlling the POC export by large rivers that integrate vast portions of the land surface, and quantify
47 the differing sources of carbon exported by those large river systems.

48 The Huanghe (Yellow River) is a highly turbid river system that exports over 85% of its OC as particulate matter,
49 with efficient deposition and preservation in the ocean (Cauwet and Mackenzie, 1993; Bianchi, 2011; Zhang et al.,
50 2013; Ran et al., 2013). The Huanghe has been highly managed over the last few decades through water and soil
51 conservation measures as well as reservoir construction, leading to a decrease of nearly 90% of its sediment load
52 (Wang and Fu et al., 2016; Wang et al., 2007; Milliman et al., 1987) and a significant decrease in its POC delivery to
53 the ocean (Zhang et al., 2013). Reservoir construction dramatically affects the transport and fate of both sediment load
54 and POC in large rivers (Syvitski et al., 2005; Li et al., 2015). The estimated POC flux of the Huanghe is thought to
55 have shifted from 4.5 Tg C/yr in the 1980s (Cauwet and Mackenzie, 1993) to 0.34-0.58 Tg C/yr nowadays (Tao et al.,
56 2018) in response to both anthropogenic influence (Hu et al., 2015; Tao et al., 2018; Yu et al., 2019a) and natural
57 variability of the regional hydrological cycle (Qu et al., 2020). These large-scale perturbations have likely modified
58 the OC input from the different terrestrial pools as well as the fate of exported POC that was previously reaching
59 deposition centers in the ocean and that now remains stuck on land. Those alterations of the carbon cycle remain to
60 be addressed.

61 Over the last decade, POC transport in the Huanghe has been investigated for 1) determination and quantification of
62 POC sources, based on bulk or molecular carbon isotopic composition (Tao et al., 2015; Yu et al., 2019b; Ge et al.,
63 2020; Qu et al., 2020); 2) temporal and spatial variations in POC export and distribution among different size fractions
64 (Ran et al., 2013; Wang 2012; 2016; Yu et al., 2019a, b ; Qu et al., 2020); 3) impact of anthropogenic activities (Hu

65 et al., 2015; Tao et al., 2018; Yu et al., 2019a); and 4) burial efficiency and preservation in the ocean (Sun et al., 2018;
66 Tao et al., 2016; Ge et al., 2020). However, all these previous studies rely on suspended sediment samples collected
67 near the channel surface or at a single, intermediate depth in the river channel, further assuming a homogeneous
68 distribution of suspended sediment characteristics in the water column, both vertically and laterally. It is now well
69 recognized that suspended sediments present physical, mineralogical, chemical, and isotopic heterogeneities across
70 river transect due to hydrodynamic sorting and tributary mixing (Galy et al., 2008b; Garzanti et al., 2010; Bouchez et
71 al., 2010, 2011a). This is also true for POC, whose age and composition vary following vertical water depth (e.g.,
72 Galy et al., 2008b; Bouchez et al., 2014; Hilton et al., 2015; Repasch et al., 2021; Schwab et al., 2022), and lateral
73 river transect (e.g., Bouchez et al., 2014; Baronas et al., 2020), and between sediment size fractions separated in the
74 laboratory (Yu et al., 2019b; Ge et al., 2020). Such heterogeneity warrants a re-evaluation of POC transport in the
75 Huanghe, accounting for the variability in suspended sediment characteristics over the channel cross-section.
76 In this study, we take advantage of in-river hydrodynamic sorting to access the full range of suspended sediment size
77 fractions by collecting suspended particulate matter (SPM) samples along several river depth profiles distributed
78 across a channel transect (e.g., Bouchez et al., 2014; Freymond et al., 2018; Baronas et al., 2020). We apply this
79 sampling scheme to a cross-section of the Huanghe located 200 km upstream from the river mouth and report SPM
80 OC content, stable isotope composition, and radiocarbon activity as well as total nitrogen, major element composition
81 (aluminum and silicon), and particle size distribution. Based on these novel samples and data sets, this study aims at
82 1) determining the controls on POC content in the Huanghe; 2) tracing and quantifying the sources of riverine POC
83 in the Huanghe; and 3) providing depth-integrated estimates of POC fluxes in the most turbid large river system.

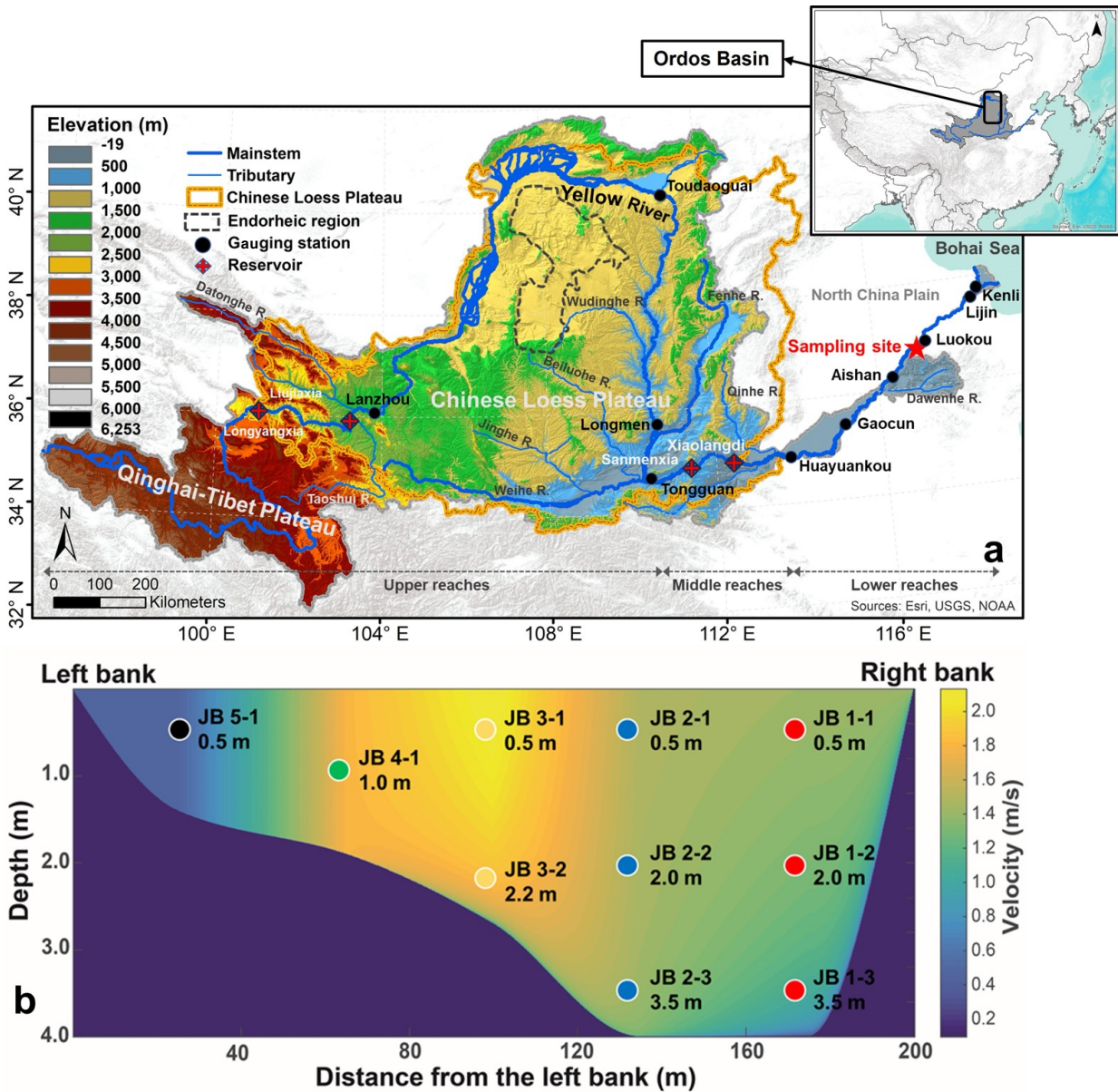
84 **2 Study area**

85 The Huanghe originates from the north-eastern Qinghai-Tibet Plateau (QTP) and runs through the Chinese Loess
86 Plateau (CLP) and the North China Plain (NCP) to the Bohai Sea (Figure 1a). It is 5,464 km long and drains a basin
87 area of 79.5×10^4 km². The Huanghe drainage basin can be subdivided into three main geomorphic units: 1) the high-
88 relief upper reaches spanning from the source region (elevation of 4,500 m) to the city of Toudaoguai (located 3,472
89 km downstream at an elevation of 1,000 m); 2) the middle reaches with a channel length of 1,206 km, ending at
90 Huayuankou (elevation of 110 m) draining landscapes characterized by relatively gentle slopes; and 3) the lower
91 reaches where the river flows eastwards across a fluvial plain over a length of 786 km. These three sections drain
92 53.8%, 43.3%, and 2.9% of the whole Huanghe basin area, respectively (Wang et al., 2007; YRCC, 2016). Most
93 second-order tributaries drain the CLP region and feed the main channel in the middle reaches, the Dawenhe River
94 being the only tributary of the lower reaches, with negligible water and sediment supply due to upstream trapping in
95 lakes and reservoirs. It is worth noting that more than 50% of the water discharge at the Huanghe's mouth comes from
96 the QTP, whereas over 90% of the sediment load originates from the CLP (Wang et al., 2010, 2017; Pan et al., 2016).
97 The CLP is thus the principal source area of sediment to the Huanghe (Shi and Shao, 2000; Guo et al., 2002; Wang
98 and Fu et al., 2016).

99 The Huanghe drainage basin is mostly underlain by the North China craton, and is bounded by several mountain belts.
100 The watershed encompasses 46% of sedimentary rock outcrops (mainly siliciclastic rocks with minor carbonates), and

101 about 45% of unconsolidated sediments (mainly Quaternary loess deposits). The remaining outcrops include
102 metamorphic, plutonic, and volcanic rocks formed from the Archean to the Tertiary (Figure S1). Although river
103 incision is strong in the QTP, a substantial part of the corresponding eroded material is not effectively transferred to
104 the lower reaches due to deposition in the CLP and the western Mu-Us desert, a situation that has prevailed since at
105 least the middle Pleistocene (Nie et al., 2015; Licht et al., 2016; Pan et al., 2016). In addition, recent anthropogenic
106 disturbance such as constructions of large dams in the upper reaches has profoundly modified the export of solid
107 materials from the basin (Wang et al., 2007). The Huanghe then flows through the CLP that has acted as the major
108 supplier of sediment to the system since at least the Calabrian Pleistocene (Stevens et al., 2013; Bird et al., 2015).
109 There, an easily erodible loess-paleosol formation has accumulated since 2.58 Ma (Guo et al., 2002), over a thickness
110 ranging from a few meters to more than 500 m, with an average of 100 m. This loess-paleosol formation and underlying
111 Cretaceous sedimentary rocks are actively incised by the main stem and its tributaries (Shi and Shao, 2000; Guo et
112 al., 2002; Wang and Fu et al., 2016). Notably, the Ordos Basin underlying the CLP is rich in oil and gas (Guo et al.,
113 2014). In the lower reaches, the river drains Quaternary fluvial deposits and sedimentary rocks.

114 The Huanghe drainage basin encompasses the entire arid and semi-arid region of northern China in the upper and
115 middle reaches, and is characterized by more humid climate conditions in the lower reaches. Annual average
116 precipitation (over the period 1950 - 2000) in the upper, middle and lower reaches regions is 368 mm, 530 mm, and
117 670 mm, respectively (Wang et al., 2007). As a result of the East Asian summer and winter monsoon circulations, the
118 rainy season (June to September) contributes 85% of the annual precipitation (Wang et al., 2007). During the rainy
119 season, frequent storm events lead to concentrated flows (relatively high discharge) in vulnerable gully-hill systems,
120 the dominant regional geomorphic landscape, and actively participates in soil erosion in the CLP (Shi and Shao, 2000;
121 He et al., 2004; Qu et al., 2020). The present-day (2002 to 2016) suspended sediment flux delivered by the Huanghe
122 to the sea is about 0.12 Gt/yr, which implies a decrease of nearly 90% in sediment export compared to the widely cited
123 estimate of 1.08 Gt/yr (average value between 1950 to 1980, Milliman and Farnsworth, 2011). This massive decrease
124 in sediment export mostly results from human perturbations, including soil conservation practices in the CLP and
125 retention in large reservoirs, rather than from climatic variations such as the decreasing precipitation observed in the
126 region over the last decades (Wang et al., 2007; Ran et al., 2013; Wang and Fu et al., 2016; Li et al., 2022). A scheme
127 for water and sediment regulation (WSR) has been implemented through the construction of the Xiaolangdi Reservoir
128 since 2002, aiming to mitigate water and sediment imbalances in the lower reaches. This regulation has resulted in a
129 modification of the flux of sediment delivered to the lower reaches and estuary, making the Huanghe a highly human-
130 regulated river system. However, no WSR was implemented in 2016, the year of our sampling campaign, suggesting
131 that the collected SPM samples are not significantly affected by retention in dams, and thus are representative of the
132 fluvial transport of terrestrial materials eroded from the CLP.



133
 134 Figure 1: (a) Elevation map of the Huanghe drainage basin showing the main reservoirs and gauging stations along the
 135 main stem as well as our sampling site (36.75°N, 117.02°E, near the Luokou gauging station); and (b) channel cross-section
 136 sampled for this study showing the depth and lateral distribution of suspended particulate matter (SPM) samples and
 137 modeled velocity distribution based on the "law of the wall", using the point velocity data measured by a current velocity
 138 meter attached to the sampler.

139 **3 Sampling and analytical methods**

140 **3.1 Sampling strategy**

141 Detailed sampling of a cross-section of the Huanghe was carried out on the 17th of July, 2016, during the flood season
 142 (Figure S2). Samples were collected along five depth profiles near the Luokou hydrological station (36.75°N, 117.02°E),
 143 250 km upstream from the river mouth (Figure 1). This sampling strategy allows for accessing the full range of
 144 suspended sediment particle size (Bouchez et al., 2014). The cross-section is 200-meters wide at the surface and 4

145 meters deep at most (Figure 1; YRCC, 2016). As in previous studies, we used a home-made, 10-liter, point-sediment
146 horizontal Niskin-type sampler attached to a current velocity meter, to collect river water samples and measure the
147 water velocity simultaneously. Subsequently, two water samples were collected at the surface near the right bank in
148 May and June 2017 before the flooding season, to retrieve fine suspended particulate matter. For each sample,
149 approximately 30 liters of river water were collected and were then filtered through pre-weighed 0.22- μm porosity
150 cellulose acetate membrane filters within 24 hours. After rinsing the filters with filtered water, all sediment samples
151 were transferred into centrifuge tubes and freeze-dried before weighing and analysis. A bed sediment (BS) sample
152 was collected on an exposed, recently flooded sediment bar of the riverbed.

153 **3.2 Physical and geochemical analysis**

154 Apart from a 50-mg aliquot of SPM samples preserved for particle size analysis, samples were finely ground using an
155 agate mortar and pestle prior to chemical and isotopic analyses. The particle size distribution of the unground aliquots
156 was measured using a Laser Diffraction Particle Size Analyzer (Beckman Coulter LS-12 320) at the École Normale
157 Supérieure (ENS), Paris, France. Before analysis, unground SPM aliquots were dispersed in deionized water and then
158 in sodium hexametaphosphate in an ultrasonic bath. For each sample, we measured three replicates and report the
159 average median particle size (D50, μm) with an uncertainty better than 2% (Table 1). The chemical composition of
160 SPM samples was measured on ground aliquots at the Centre de Recherches Pétrographiques et Géochimiques
161 (CRPG), Vandoeuvre-lès-Nancy, France, using inductively coupled plasma atomic emission spectroscopy (ICP-OES)
162 for major elements with typical uncertainties of 3% (Carignan et al., 2001).

163 For particulate organic carbon content (POC%, wt.), stable carbon isotope $\delta^{13}\text{C}$ (in ‰_{VPDB}, *i.e.*, in ‰ relative to Vienna
164 Pee Dee Belemnite) and radiocarbon isotope $\Delta^{14}\text{C}$ (expressed as fraction modern, Fm), ground homogenized samples
165 were fumigated using 12M HCl fumes in a closed Teflon tank at 60 °C for 48 hours to remove the carbonate fraction,
166 and were then dried under vacuum prior to analysis. Total nitrogen content (TN%, wt.) was measured on non-acidified
167 samples (Komada et al., 2008). Triplicate analysis on POC% and $\delta^{13}\text{C}$ of POC (acidified aliquots) as well as TN%
168 (non-acidified aliquots) were carried out on an Organic Elemental Analyzer (OEA) coupled with Isotope Ratio Mass
169 Spectrometry (IRMS, Thermo Scientific Flash 2000) under continuous flow mode at Géosciences Paris Saclay
170 (GEOPS), Orsay, France. Subjected to the blank subtraction by linearity test, two international standards including
171 USGS-40 and IAEA-600 as well as an internal standard (GG-IPG) were used to build linear regression equations to
172 calibrate the elemental and isotopic values for both carbon and nitrogen. Uncertainties on POC%, $\delta^{13}\text{C}$, and TN%,
173 based on replicate measurements (1σ , $n=3$), are lower than 0.02%, 0.06‰, and 0.02‰, respectively. The ^{14}C activity
174 of POC was measured on a new compact accelerator mass spectrometry (AMS), *ECHoMICADAS* (Hatté et al., 2023),
175 using a gas ion source interface system (GIS) at the Laboratoire des Sciences du Climat et de l'Environnement (LSCE),
176 Gif-sur-Yvette, France, with an absolute uncertainty of max $\pm 0.5\%$. Aside from the gas bottles of prepared blank PhA
177 and standard NIST OX II which are permanently connected to the GIS and, used for normalization and corrections for
178 fractionation and background, international standards including IAEA-C5, IAEA-C7, IAEA-C8, and blank PhA were
179 prepared in different sizes (10 to 100's $\mu\text{g C}$) to match the amount of OC found in the sediment samples.

180 3.3 POC source apportionment

181 To quantify the contribution and associated uncertainties of various sources to POC transported in the Huanghe, a
182 Bayesian Markov Chain Monte Carlo (MCMC) based on a three-end member (Appendix A) mixing scheme was
183 adopted. This approach considers the variability on each end member contribution, assuming this variability can be
184 represented by a normal distribution. Prior information is assumed to be uninformative. We computed the *a posteriori*
185 distribution of the Bayesian formulation using the MCMC method, using the MixSIAR package (Moore & Semmens,
186 2008; Stock & Semmens, 2016). All computations were performed in the R environment (<http://www.r-project.org/>).
187 To ensure reliable simulation, the model was run with chain length of 300,000 by 3 chains, using a burn-in of 200,000
188 steps, and a data thinning of 100 for each sample. The mixing model was constructed on the dual stable and radioactive
189 isotope of the riverine POC pool ($\delta^{13}\text{C}$ and $\Delta^{14}\text{C}$) and of the three potential source pools (Section 5.2) by the following
190 equations:

$$191 \quad \text{Isotope_ratio}_{\text{sample}} = \sum_{\text{source}} (f_{\text{source}} * \text{Isotope_ratio}_{\text{source}})$$
$$192 \quad \sum_{\text{source}} f_{\text{source}} = 1$$

193 where $\text{Isotope_ratio}_{\text{sample}}$ is either the $\delta^{13}\text{C}$ or $\Delta^{14}\text{C}$ value of the sample, $\text{Isotope_ratio}_{\text{source}}$ is either the $\delta^{13}\text{C}$ or
194 $\Delta^{14}\text{C}$ value of different possible sources of POC and f_{source} is the relative contribution of each source of POC. Further
195 model diagnostics was performed using Gelman-Rubin and Geweke test, both diagnostics validated the robustness
196 and convergency of the model.

197 3.4 Depth-integrated fluxes

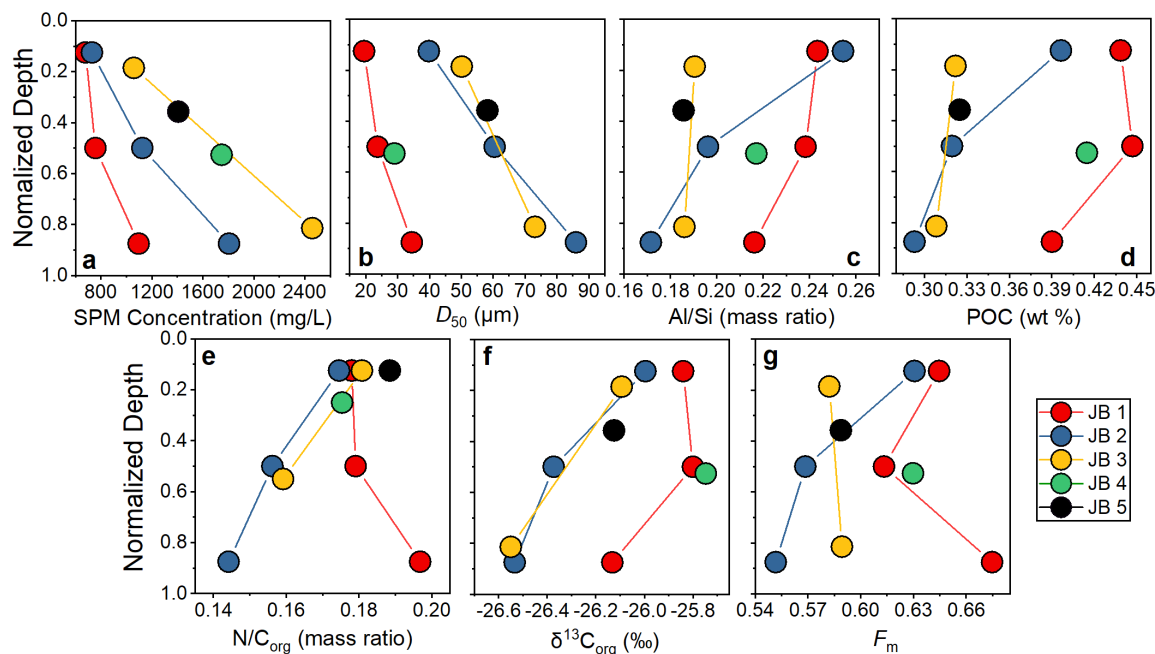
198 Instantaneous depth-integrated fluxes of SPM and POC sources were calculated for the cross-section using a method
199 developed by Bouchez et al. (2011a, b). This method is based on the systematic variation of SPM concentration in the
200 water column (Figure 2) applying a Rouse-based model (Rouse, 1937). We first constructed a bathymetric profile of
201 the river cross-section based on the depth information collected in the field and then modeled the velocity distribution
202 across the transect (Figure 1b) through fits of the so-called "law of the wall" to water velocity measured at the location
203 of each sample within the cross-section using a current meter. Afterward, the concentration of total SPM and various
204 particle size fractions could be estimated by applying the so-called Rouse model (Rouse, 1937) to each particle size
205 fraction separately (Bouchez et al., 2011a), resulting in a map of the particle size distribution in the river cross-section
206 (Figure S3). The aluminum to silicon ratio (Al/Si mass ratio) is inversely related to the particle size of river SPM in
207 the Ganges-Brahmaputra, the Amazon, and the Mackenzie Rivers (Galy et al., 2007; Bouchez et al., 2014; Hilton et
208 al., 2015). Such a linear relationship between D50 and Al/Si was also observed in our dataset, allowing for computing
209 the spatial distribution of POC content in the cross-section, based on the linear relationship between POC and Al/Si
210 (Figure 3). Finally, combining modeled water velocity, SPM concentration, and POC distribution we calculated a
211 depth-integrated, instantaneous POC flux for the whole river channel (Figure S3, detail in supplementary material).

212 4 Results

213 We report the first isotopic dataset of POC samples collected along several depth profiles distributed over a cross-
214 section of the Huanghe (Table 1, n=10). SPM concentrations range from 679 to 2,459 mg/L (avg. $1,286 \pm 572$ mg/L,
215 reported with mean value with one standard deviation, herein after) and show an obvious increase from the surface to
216 the bottom and from the right bank to the left bank (Figure 1b and 2a). The surface SPM concentration (*i.e.*, samples
217 collected 0.5 m below the surface) decreases laterally as the water column deepens. The range of measured Huanghe
218 SPM D50, *i.e.* the median particle size (19.5-86.0 μm , Figure 2b) agrees with that of SPM collected at Lijin (16.6-
219 120.1 μm , n=50) during the same flooding season by Moodie et al. (2022). In each depth profile, SPM is consistently
220 coarsening with depth as revealed by the evolution of grain size parameters such as D10, D50, and D90 (Table 1,
221 Table S1, Figure 2 and Figure S4). The finest SPM is transported on the right bank and at the surface, while the
222 coarsest SPM is found at the bottom of the middle profile (sample JB 2-3). Two types of depth profiles can be
223 distinguished at Luokou based on particle size distributions (Figure S4) and the relationship between D50 and water
224 depth (Figure 2b). On the one hand, the JB 1 and JB 4 profiles show a well-marked, bi-modal distribution of particle
225 size (Figure S4) together with relatively low and consistent D50 (Figure 2b). On the other hand, the JB 2, JB 3, and
226 JB 5 profiles show a more unimodal distribution of particle size (Figure S4) and a unique D50 - sampling depth
227 relationship (Figure 2b). Interestingly, these two groups can also be distinguished in terms of relationships between
228 POC% and $\delta^{13}\text{C}$ with water depth (Figures 2d, 2f). As expected, the Al/Si ratio is well-related to the particle size, and
229 the ratios measured in the middle profile SPM samples (0.17 for JB 2-3 and 0.26 for JB 2-1) encompass the full range
230 of Al/Si found in the whole cross-section (Figure 2c). The relatively low Al/Si ratios are comparable to that of the
231 middle Huanghe (Qu et al., 2020) and other large turbid river systems such as the Ganges-Brahmaputra (Galy et al.,
232 2008b), Salween, and Irrawaddy (Tipper et al., 2021).

233 SPM in the Huanghe is characterized by low TN and POC content (wt.%), ranging from 0.04% to 0.08% ($0.06 \pm$
234 0.01%) and from 0.29% to 0.42% ($0.37 \pm 0.06\%$), respectively (Figure 2d; Table 1). POC content generally decreases
235 from the surface to the river bed, with quantitative differences from one profile to another (Figure 2d). Notably, the
236 JB 1 profile shows the highest POC% and TN%. In addition, the ratio of TN% to POC%: $\text{N}/\text{C}_{\text{org}}$ increases with depth
237 in the JB 1 profile (from top to bottom), while it decreases in the JB 2 and JB 3 profiles (Figure 2e). The $\delta^{13}\text{C}$ of POC
238 varies over a narrow range from -26.55% to -25.75% ($-26.12 \pm 0.29\%$, Figure 2f) and becomes lighter with depth,
239 showing that fine SPM has higher $\delta^{13}\text{C}$ than coarse SPM. These values are lower than those previously reported for
240 other Huanghe sampling sites upstream: $-24.7 \pm 0.4\%$ at Toudaoguai, $-24.9 \pm 0.6\%$ at Longmen, and $-23.8 \pm 0.6\%$
241 at Lijin (Qu et al., 2020, Hu et al., 2015; Tao et al., 2015; Yu et al., 2019a; Ge et al., 2020). The radiocarbon activity
242 of POC of the Huanghe at Luokou is relatively low (Figure 2g), with F_m ranging from 0.552 ($\Delta^{14}\text{C} = -453\%$; sample
243 JB2-3) to 0.675 ($\Delta^{14}\text{C} = -331\%$; sample JB1-3), spanning from 3,160 to 4,780 ^{14}C yrs, and the average value is 0.607
244 ± 0.038 ($\Delta^{14}\text{C} = -412 \pm 37.6\%$, n=10). This range of radiocarbon activity is consistent with published values for POC
245 collected at the river surface downstream of Toudaoguai (Qu et al., 2020). All the POC radiocarbon activity data
246 reported so far for the Huanghe are comparable to mean values for Arctic large rivers ($\Delta^{14}\text{C} = -397\%$, ca. 4,480 ^{14}C
247 yrs, Ke et al., 2022), revealing the multimillennial-age nature of POC transported by the Huanghe. The elemental and
248 isotopic signatures of the two fine SPM samples HH 17.05 and HH 17.06 (on average POC% = 1.07%, $\delta^{13}\text{C} =$

249 -25.67% , $F_m = 0.720$; and $Al/Si = 0.37$) are significantly different from those of the depth profile samples (Table 1).
 250 The bed sediment sample has a comparatively low POC% (0.21%), $\delta^{13}C$ (-27.35%), F_m (0.099), and Al/Si ratio
 251 (0.17).



252
 253 **Figure 2: Variation of physical and chemical parameters in the river cross-section, shown as a function of sampling depth**
 254 **normalized to total depth of the water column at the location of the considered depth-profile, for the Luokou cross-section**
 255 **on the Huanghe (June 16, 2017). (a) SPM concentration; (b) particle size distribution (shown as D50); (c) Al/Si mass ratio;**
 256 **(d) POC content (weight %); (e) N/C_{org} mass ratio; (f) stable carbon isotope ratio $\delta^{13}C_{org}$ (‰); (g) radiocarbon activity F_m .**

257 **Table 1: SPM characteristics and POC properties of the river-cross-section sampling.**

Sample ID	Type	Depth (m)	SPM mg/L	POC (%)	SD	$\delta^{13}C_{org}$ (‰)	SD	F_m	$\Delta^{14}C$ (‰)	SD	^{14}C age	TN (%)	N/C _{org}	Al/Si	D50 μm
JB 1-1	SPM	0.5	679	0.44	0.02	-25.84	0.03	0.645	-360	7	3527	0.078	0.178	0.243	19.5
JB 1-2	SPM	2	757	0.45	0.01	-25.80	0.06	0.613	-392	11	3929	0.080	0.179	0.238	23.7
JB 1-3	SPM	3.5	1095	0.39	0.01	-26.13	0.04	0.675	-331	7	3161	0.077	0.197	0.216	34.5
JB 2-1	SPM	0.5	730	0.40	0.03	-26.00	0.01	0.631	-374	7	3703	0.069	0.175	0.255	39.8
JB 2-2	SPM	2	1124	0.32	0.01	-26.37	0.06	0.569	-436	13	4537	0.050	0.156	0.196	60.4
JB 2-3	SPM	3.5	1806	0.29	0.01	-26.53	0.06	0.552	-453	38	4779	0.042	0.144	0.172	86.0
JB 3-1	SPM	0.5	1058	0.32	0.02	-26.09	0.03	0.582	-422	12	4346	0.058	0.181	0.190	50.1
JB 3-2	SPM	2.2	2459	0.31	0.02	-26.55	0.04	0.589	-415	11	4247	0.049	0.159	0.186	73.1
JB 4-1	SPM	1	1747	0.41	0.02	-25.75	0.06	0.630	-375	8	3714	0.073	0.175	0.217	29.0
JB 5-1	SPM	0.5	1406	0.32	0.01	-26.12	0.05	0.589	-416	11	4256	0.061	0.188	0.186	58.2
HH 17.05	SPM	0	83	0.92	0.00	-25.73	0.14	0.711	-295	19	2740	0.184	0.200	0.358	5.2
HH 17.06	SPM	0	54	1.21	0.01	-25.60	0.07	0.729	-277	25	2539	0.261	0.215	0.377	4.3
HH	BS			0.21	0.03	-27.35	0.05	0.099	-901	7	18539	0.019	0.087	0.175	44.4

258 5 Discussion

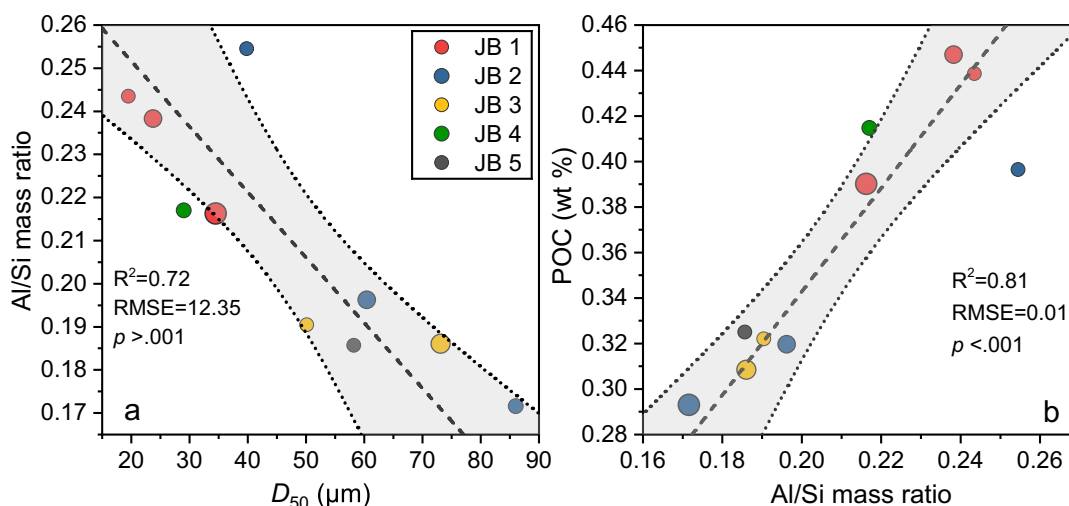
259 We observe significant heterogeneities of elemental and isotopic carbon composition as well as inorganic chemistry
 260 over the studied river cross-section. The possible mechanisms behind these variations are assessed hereafter. Then,
 261 sources of riverine POC are determined and quantified, confirming that erosion of the loess-paleosol sequence of the

262 CLP is a major source of aged and refractory biospheric OC to the Huanghe. Finally, we assess the POC load and its
 263 variability over the transect profile, inferring the importance of the supply of POC from the river bottom in the
 264 Huanghe.

265 5.1 Transportation mode of POC in the Huanghe

266 5.1.1 POC loading and its controls

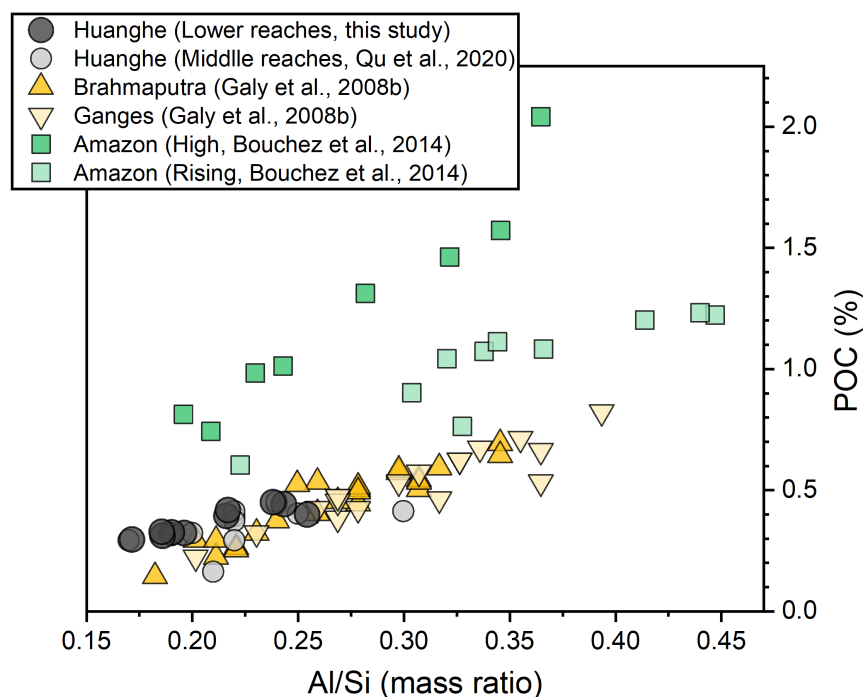
267 The Huanghe is characterized by a high SPM load with relatively low POC% ($0.37 \pm 0.06\%$, $n=10$). In the Luokou
 268 cross-section, POC content generally increases with decreasing particle size (Figure S5), with the two clay-sized
 269 ("HH") samples showing the largest POC content (Table 1). Consistently, the Al/Si ratio of Huanghe sediments, which
 270 varies as an inverse linear function of the median particle sizes D_{50} ($R^2=0.72$, $p > .001$, Figure 3a), positively correlates
 271 with POC% ($R^2=0.81$, $p < .001$ Figure 3b), a pattern observed globally (Galy et al., 2008b; Bouchez et al., 2014; Hilton
 272 et al., 2015; Repasch et al., 2021). This pattern is consistent with POC variability in the Huanghe reported for manually
 273 separated size fractions of sediments (Yu et al., 2019b).



274
 275 **Figure 3: Relationships between (a) particle size D_{50} and Al/Si mass ratio; (b) Al/Si mass ratio and POC content for the**
 276 **Luokou cross-section on the Huanghe (July 17, 2016). The symbol size indicates the sampling depth in the water column,**
 277 **with symbol size increasing with depth. The shaded area represents the 95% confidence area of the linear best-fit (black**
 278 **dashed line), the upper and lower bound are marked by grey dotted lines.**

279 The first reason for the low POC content of Huanghe sediments is therefore their relatively low values of Al/Si
 280 compared to other systems - a feature than can be related to the quartz-rich, OC-poor nature of the loess-paleosol
 281 formations of the CLP (Jahn et al., 2021; Huang and Ren, 2006; He et al., 2006; Ning et al., 2006; Wang and Fu,
 282 2016). However, Huanghe sediments are relatively poor in POC, even considering their low Al/Si, compared to other
 283 rivers globally. To that effect, the so-called "POC loading" can be characterized by the slope described by sediment
 284 data in an Al/Si-POC diagram (Galy et al., 2008b; Figure 4). For a given Al/Si ratio, the POC% in the Luokou cross-
 285 section is similar to that of the middle Huanghe (Qu et al., 2020), indicating the relatively invariant transport mode of
 286 POC between the middle and lower reaches. Previous studies have shown that the positive relationship between POC%
 287 and Al/Si can be partially explained by OC adsorption onto the mineral surface (Curry et al., 2007; Galy et al., 2008b;
 288 Blair and Aller, 2012; Bouchez et al., 2014; Qu et al., 2020). In the loess-paleosol deposits acting as a source of

289 sediments to the Huanghe, OC is mostly preserved and stabilized by forming organo-aggregates with kaolinite and
 290 through adsorption onto iron oxides (Wang et al., 2013).
 291 However, POC loading in the Huanghe is small compared to that of the Amazon (Bouchez et al., 2014), but similar
 292 to that of the Ganges-Brahmaputra system (Galy et al., 2008b). While many factors could influence POC loading
 293 across these catchments, we note that another similarity between the Huanghe and Ganges-Brahmaputra fluvial
 294 systems is their millennial-aged OC_{bio} (Galy et al., 2007; Tao et al., 2016). This is in stark contrast with the Amazon,
 295 where younger OC_{bio} ages have been reported (Bouchez et al., 2014). Given that younger OC_{bio} recently
 296 photosynthesized in terrestrial or aquatic ecosystems can be readily oxidized within catchments (Mayorga et al., 2005),
 297 the relatively low POC loading observed at the mouth of the Ganges-Brahmaputra and the Huanghe (Figure 4) could
 298 be related to the predominance of refractory, aged OC_{bio} and OC_{petro} in those systems, while the Amazon sediments
 299 would still contain significant amount of younger, more labile OC_{bio} .



300
 301 **Figure 4: "POC loading" of river SPM of large rivers. The POC loading is estimated from the slope of the relationship**
 302 **between POC content and the Al/Si ratio of each fluvial system (Galy et al., 2008b). All SPM samples were collected along**
 303 **depth profiles except for the middle Huanghe (Qu et al., 2020).**

304 In detail, and as explained in more detail below (**Section 5.1.2**) we also observe a significantly different POC loading
 305 between the JB 1 and JB 2 depth profiles at the Luokou station (Figure 3). This difference in POC loading in the cross-
 306 section of the Huanghe might indicate the delivery of recent OC_{bio} , specifically near the right bank (the closest to the
 307 JB 1 profile) for the Luokou site, a scenario which is supported by the comparatively younger age of POC in profile
 308 JB 1. Consistently with this interpretation, temporally variable POC loading at a given site has been reported for the
 309 Amazon (Bouchez et al., 2014), where higher POC loading during the high-water stage compared to the rising water
 310 stage has been attributed to the erosion of discrete organic debris from riverbanks.

311 Variable POC loading amongst large catchments has implications for evaluating the likelihood of POC preservation
 312 in estuaries. The Ganges-Brahmaputra system delivers relatively old, refractory OC_{bio} to the Bengal Fan with an almost

313 complete burial efficiency (Galy et al., 2007). Given the observed similarity in POC loading and age, we can thus
314 expect a similar, efficient preservation for the Huanghe offshore depositional system. In addition to the low reactivity
315 of the POC transported by the Huanghe, the high sediment accumulation rates in the Huanghe coastal domain might
316 further inhibit OC oxidation (Blair and Aller, 2012). Consequently, the case of the Huanghe differs drastically from
317 that of the Amazon, where higher POC loading is observed, with a larger contribution of young, labile OC_{bio} either as
318 discrete organic matter or associated with mineral surfaces, leading to low POC burial efficiency in the ocean
319 (Bouchez et al., 2014; Blair and Aller, 2012).

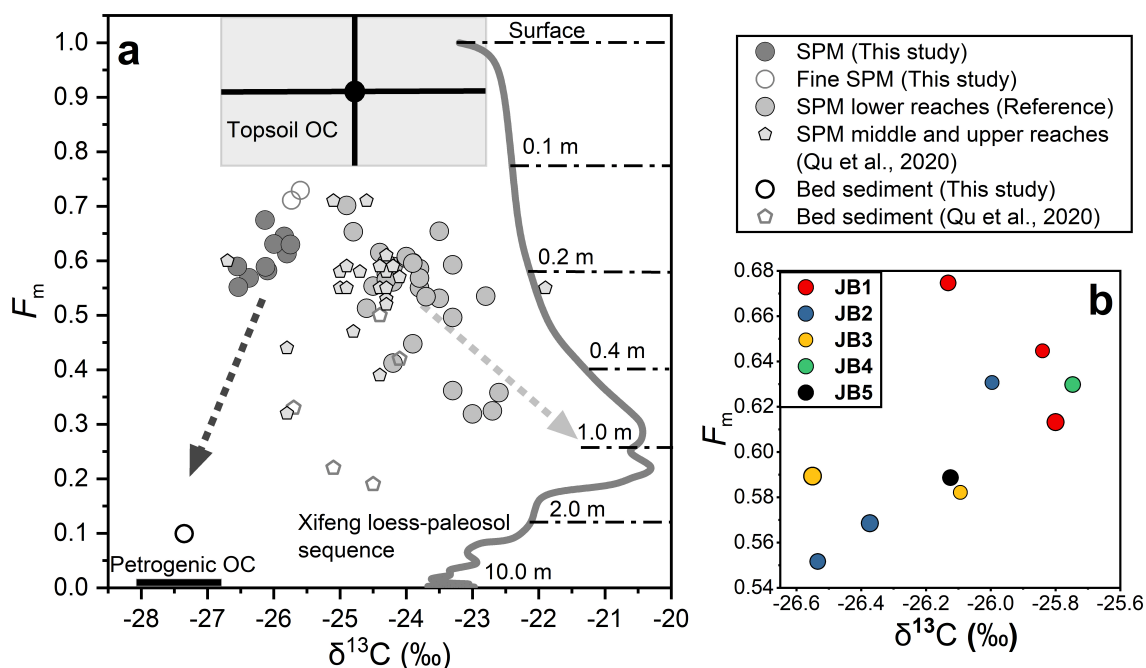
320 **5.1.2 Chemical heterogeneity within the transect**

321 There is clear lateral and vertical variability of POC content and SPM inorganic chemistry across the Luokou cross-
322 section of the Huanghe. For each vertical depth profile, clay-rich fine particles are transported near the channel surface,
323 and quartz-rich coarse particles flow near the river bottom. Accordingly, the Al/Si ratio, POC content and POC
324 radiocarbon activity generally decrease with depth. Elemental (POC%) and isotopic POC signatures (¹³C and ¹⁴C) are
325 inversely related to the particle size (D₅₀; Figure S5). These patterns are observed in other large fluvial systems, e.g.,
326 Ganges and Brahmaputra, Amazon and Mackenzie (Galy et al., 2008b; Bouchez et al., 2014, Hilton et al., 2015),
327 showing that hydrodynamic sorting is the primary control on suspended sediment OC content, segregating inorganic
328 and organic material according to particle size (Bouchez et al., 2011a, 2014).

329 At the Luokou sampling site, lateral variability at the channel surface shows that POC-rich fine particles are
330 preferentially transported near the right bank (Figure 2 and Figure S3). This pattern is validated by the Rouse model
331 provided in Text S1, the Rouse number (Z_R) is 0.137, 0.236, and 0.284 for JB-1, JB-2, and JB-3, respectively. In
332 essence, Z_R can reflect the balance between gravitation settling and upward turbulent diffusion. Z_R is smaller near the
333 right bank while larger near the left bank, showing heterogeneity across the transect. Larger particles exhibit a faster
334 settling velocity due to their increased weight, leading to a higher Z_R . On the other hand, the lighter ones settle more
335 slowly, resulting in Z_R approaching 0. This means that their concentration remains relatively constant along a given
336 depth profile. However, as depth increases and the concentration of larger particles grows, the proportion of these
337 finer particles in the overall sediment decreases (Bouchez et al., 2011a). The channel geometry thus needs to be
338 examined as a potential factor to produce such lateral heterogeneity, in particular the mechanisms of bed sediment
339 resuspension and bank erosion.

340 Resuspension of bed sediments is also a possible mechanism that could explain the lateral heterogeneity in POC
341 content in the study cross-section of the Huanghe. Indeed, scouring of channel bed sediment at high water flow may
342 also shift POC to more negative radiocarbon and stable isotope signatures. Our sample set collected in July 2016
343 during a flooding period (water flow velocity up to 2.1 m/s, Figure 1) supports this scenario. Indeed, the increase in
344 D₅₀ of surface SPM samples from right to the left bank, that is with total channel depth decrease, is consistent with
345 coarse sediment resuspension from the bed. This is also supported by the Rouse model, where higher Z_R in the shallow
346 water near the left bank indicates a greater likelihood of sediment settling to the bed, lower Z_R suggests that there is
347 enhanced SPM supply from the riverbed. Such a scenario is also supported by the three-fold increase in SPM flux

348 observed from the upstream Huayuankou station to the downstream Lijin station in July 2016, despite a four-fold
 349 decrease in water discharge (Figure S2).
 350 Bank erosion can be a significant mechanism for the delivery of sediments to river systems (Guo et al., 2007). Bank
 351 erosion at Luokou would make OC from the lower Huanghe alluvial plain a potential source of POC in the lower
 352 reaches of the Huanghe. Frequent inundation to the adjacent riparian zones in flooding seasons, surface runoff driven
 353 by storm events, and agriculture irrigation etc., can mobilize young soil OC and discrete organic matter debris (*e.g.*,
 354 plant-driven debris) to riverine POC (Hilton et al., 2011; Turowski et al., 2016). This mechanism provides a possible
 355 explanation for the opposite trends displayed by samples from the JB 1 and JB 2 profiles in the F_m vs. $\delta^{13}C$ space
 356 (Figure 5). The youngest POC was found at the bottom of the JB 1 profile (JB 1-3). Meanwhile, the JB 1 samples have
 357 comparatively higher N/C_{org} ratios and $N\%$, consistent with the input of discrete plant-derived debris from the bank
 358 in addition to rock-derived detrital clastic material in the coarse fractions ($> 32 \mu m$, Yu et al., 2019b). The transport
 359 and entrainment of plant debris deep in the water column has been evidenced in many large river systems, such as the
 360 Amazon (Feng et al., 2016), the Ganges-Brahmaputra (Lee et al., 2019), the Mackenzie (Schwab et al., 2022), the Rio
 361 Bermejo River (Repasch et al., 2021). Such input would also provide an explanation for the higher POC loading of
 362 the JB 1 profile (Section 5.1.1).



363
 364 **Figure 5:** (a) ^{14}C activity (expressed as F_m) vs. $\delta^{13}C$ for a compilation of POC data collected over the 2011-2016 period in
 365 the lower Huanghe, including samples from this study and previous studies at Huayuankou, Lijin, and Kenli (Hu et al.,
 366 2015; Tao et al., 2015; Yu et al., 2019a; and Ge et al., 2020); SPM and bed sediment (BS) collected by Qu et al., 2020 at
 367 Toudaoguai (most downstream location of the upper reaches) and Longmen in the middle reaches (Table S1). The grey
 368 curve corresponds to $\delta^{13}C_{org}$ of the top 10 m of the Xifeng loess-paleosol (Ning et al., 2006), and the corresponding F_m was
 369 calculated from ^{10}Be -derived ages following 'Age = $-8033 * \ln(F_m)$ '. The soil depth is marked above the dot-dash line (Zhou
 370 et al., 2010). Topsoil OC represents OC from the upper 10 cm of the loess-paleosol sequence with standard deviation marked

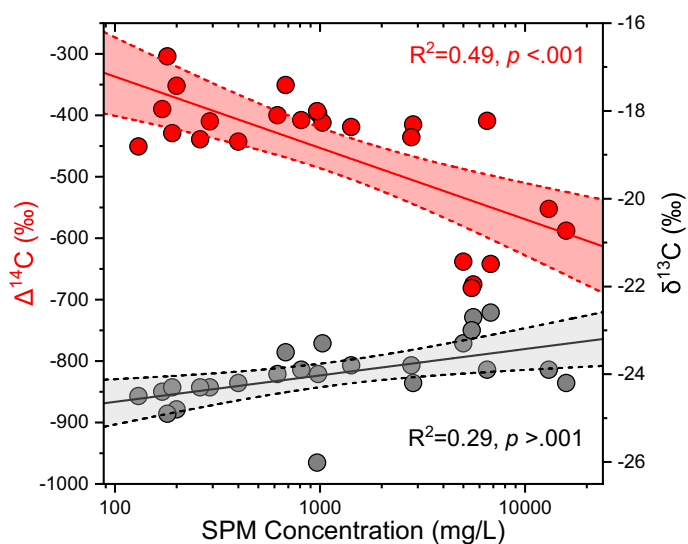
371 with black lines. (b) ^{14}C activity (expressed as Fm) vs. $\delta^{13}\text{C}$ diagram for the Huanghe sediment samples collected in this
372 study at the Luokou cross-section. Symbol size increases with sampling depth in the water column.

373 5.2 POC provenance in the Huanghe: the significance of loess-paleosol-derived OC

374 5.2.1 Physical erosion of the loess-paleosol sequence

375 Over decennial to centennial time scales, the POC export of the Huanghe is mainly controlled by erosion of the CLP.
376 Throughout the Quaternary, the erosion rate in the Huanghe basin has been mainly driven by climate shifts until human
377 activities started and profoundly impacted sediment fluxes in the mid-Holocene (He et al., 2006). The Huanghe has
378 experienced a 90% decrease in annual sediment load since the 1950s (Wang et al., 2015), caused by weakened soil
379 erosion to the CLP and sediment retention by dams (Wang et al., 2007; Ran et al., 2013; Wang and Fu et al., 2016; Li
380 et al., 2022). To determine the contributions of the various terrestrial OC components to Huanghe POC, we compiled
381 published POC carbon isotope data for sediments collected in the lower reaches from 2011 to 2016, after the
382 Xiaolangdi Reservoir was operated (Figures 5 and 6). This dataset shows that the radiocarbon ages of Huanghe POC
383 are considerably old ($5,100 \pm 1,700$ ^{14}C yrs, $n=29$), with a minor fraction of modern photosynthesized OC_{bio} (Tao et
384 al., 2015; Yu et al., 2019a, b). This relatively ^{14}C -depleted POC suggests the significant contribution of OC originated
385 from deep soil horizons within the catchment. Given that loess is easily erodible and that there is widespread gully
386 erosion in the catchment, more intensive erosion of the CLP can mobilize more soils as well as older OC from deep
387 soil horizons to fluvial transport. Therefore, higher sediment load in the river can be characterized by radiocarbon-
388 depleted POC. This is evidenced by the negative trend between ^{13}C and Fm of POC for sediment samples collected in
389 the Huanghe over the 2011-2016 period (Figure 5a), suggesting that deep horizons of the loess-paleosol formations
390 are a plausible source for the ^{14}C -depleted end member. Besides, the preferential erosion of bomb carbon affected,
391 recently photosynthesized and possibly degraded OC_{bio} from the overlying topsoils (< 10 cm) most likely contributes
392 to riverine POC (Tao et al., 2015).

393 As such, variable contribution of aged and radiocarbon-free OC from deep horizons of loess-paleosol formations of
394 the CLP should have a significant impact on the elemental and isotopic signature of POC in the lower Huanghe.
395 Erosion of loess-paleosol can also explain the decreasing POC% with increasing SPM concentration at different sites
396 of the main channel (Ran et al., 2013; Qu et al., 2020), the negative relationship between SPM concentration and
397 corresponding POC Fm at Luokou ($R^2=0.49$, $p < .001$, Figure 6), and the low POC loading of the Huanghe (Section
398 5.1.1), as the deep horizons of the loess-paleosol sequences are OC-poor, and mostly host OC that is highly degraded
399 and refractory (Liu et al., 2012; Wang et al., 2013; Cheng et al., 2020). However, the slight increase of POC $\delta^{13}\text{C}$ with
400 increasing SPM concentration ($R^2=0.29$, $p > .001$) might indicate a significant supply of soil OC from loess-paleosol
401 shallower depth, as inferred from the $\delta^{13}\text{C}$ variation within the Xifeng loess-paleosol sequence (Figure 5a).



402
 403 **Figure 6:** ^{14}C activity (expressed as $\Delta^{14}\text{C}$; red circles) and $\delta^{13}\text{C}$ (grey circles) of POC vs. SPM concentration for surface
 404 samples from the Huanghe collected from 2011 to 2016 (average SPM concentration of surface samples in this study and
 405 from Hu et al. (2015), Tao et al. (2015), Yu et al. (2019a), and Ge et al. (2020)). These paired dual carbon isotope data
 406 corresponds to the group ‘SPM lower reaches’ in Figure 5. Straight lines correspond to best-fit logarithmic curves, and
 407 shaded areas represent the 95% confidence interval.

408 The $\text{N}/\text{C}_{\text{org}}$ ratio provides additional evidence for the significant contribution of loess-paleosol material to Huanghe
 409 POC (Figure S6). Indeed, the $\text{N}/\text{C}_{\text{org}}$ ratios of SPM collected in the lower reaches ranges from 0.10 to 0.23 (this study,
 410 Ran et al., 2013; Yu et al., 2019a), whereas topsoils of the CLP are characterized by $\text{N}/\text{C}_{\text{org}}$ lower than 0.14 (Liu and
 411 Liu, 2017) and sedimentary rocks typically have very low $\text{N}/\text{C}_{\text{org}}$ (Hilton et al., 2015). Soil OC input from the North
 412 China Plain is also unlikely given its $\text{N}/\text{C}_{\text{org}}$ of 0.10-0.13 (Shi et al., 2017). Therefore, all these possible sources cannot
 413 explain the high $\text{N}/\text{C}_{\text{org}}$ signatures of riverine SPM. In addition, the high turbidity of the Huanghe ($> 600 \text{ mg/L}$) during
 414 the sampling season is likely to inhibit *in-situ* primary production ($\text{N}/\text{C}_{\text{org}} > 0.13$) (Zhang et al., 2013; Hu et al., 2015).
 415 As a result, only soil OC from deep loess-paleosol horizons appears as a plausible supplier to downstream Huanghe
 416 POC, given the high $\text{N}/\text{C}_{\text{org}}$ ratios previously reported for various loess-paleosol sequences (Figure S6, Ning et al.,
 417 2006).

418 Geomorphic processes in the CLP region support the erosion of deep soil horizons. There, gully erosion is thought to
 419 be responsible for more than 80% of the total sediment yield in the CLP (He et al., 2006; Li et al., 2022). Gullies are
 420 densely distributed and cover about 42% of the total area of the CLP and up to 60% in hilly regions (Huang and Ren,
 421 2006; He et al., 2006). Nowadays, the well-developed gully geomorphic system of the CLP is characterized by gullies
 422 with a depth of about 10 m on average and represents the most active vertical and regressive erosion of loess (Huang
 423 and Ren, 2006). This incision process erodes all types of unconsolidated materials, including the loess-paleosol
 424 sequence, underlying red clays, and colluvial deposits in the form of creeps, falls, and slides in the watershed (Zhu,
 425 2012). From 1925 to 1981, the erosion rate of the CLP was $6,318 \text{ t km}^{-2} \text{ yr}^{-1}$, compared to $10,770 \text{ t km}^{-2} \text{ yr}^{-1}$ in the
 426 hilly and gully plateau (Li et al., 2022). While the CLP's erosion rate dropped to $3,476 \text{ t km}^{-2} \text{ yr}^{-1}$ between 1982 and
 427 2016, the rate in the hilly and gully plateau remained significantly high at $6,146.5 \text{ t km}^{-2} \text{ yr}^{-1}$ (Li et al., 2022). All these

428 observations suggest that gully erosion can strongly impact the composition of riverine POC. As gully erosion is
 429 sensitive to climate change and anthropogenic activities, soil dynamics in the Huanghe basin have been altered since
 430 the mid-Holocene (He et al., 2006; Li et al., 2022). Notably, the strengthening of the East Asian Monsoon in coming
 431 decades (Li et al., 2022; Xue et al., 2023) could potentially enhance this process. However, in recent years, soil and
 432 water conservation and environmental rehabilitation campaigns (Wang et al., 2007) largely contributed to the
 433 reduction of SPM export by the Huanghe with a transfer to the estuary of 10.6 Mt in 2016, which is one order of
 434 magnitude lower than the annual sediment flux measured in 2013 (172.8 Mt) and two orders or magnitude lower
 435 compared to the flux of the 1950s (*ca.* 1,340 Mt; Wang et al., 2015). This sediment load reduction is consistent with
 436 the weakened erosion rate observed in the CLP, such modifications should thus have drastically inhibited the OC
 437 mobilization from the CLP and the POC export by the Huanghe.

438 5.2.2 POC source determination and end member apportionment

439 Considering the SPM geochemistry and the basin characteristics, three terrestrial sources can be identified as necessary
 440 to form the composition of the Huanghe POC at the Luokou cross-section. As discussed in Section 5.2.1 and shown
 441 in Figure 5a, two of these sources are (a) topsoil-derived OC (OC_{ts}) and (b) OC from deeper horizons of the loess-
 442 paleosol sequence (OC_{lps}) excluding topsoil. In addition, at the Luokou cross-section, bed OC shows lower F_m and
 443 $\delta^{13}C$ values compared to that of SPM, suggesting a significant contribution of (c) rock-derived OC from erosion in the
 444 middle reaches (OC_{petro}).

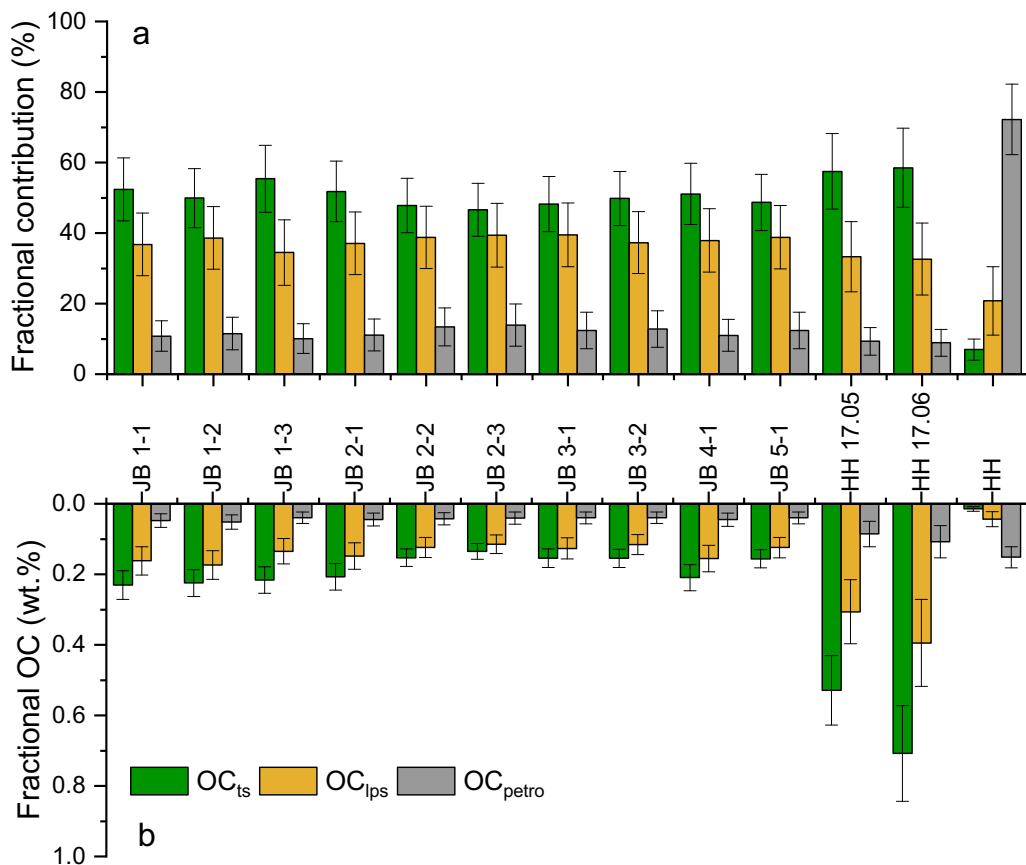
445 We adopted a Bayesian Monte-Carlo model to reconstruct source apportionment based on the mass balance of carbon
 446 isotopes ($\delta^{13}C$ and $\Delta^{14}C$) of our three defined end members (Section 3.3, Table. 2, Appendix A). The mixing space
 447 showing the geometric area between three end members is shown in Figure S7. Modeling results are shown in Figure
 448 7 as relative contributions (Figure 7a) and weight percentage (Figure 7b) of OC_{ts} , OC_{lps} , and OC_{petro} (Table S2). The
 449 contribution of OC_{petro} to total Huanghe POC at Luokou varies between 10.1% and 13.9% in the cross-section, which
 450 is higher than the contribution calculated for in the two fine SPM samples (avg. $9.1 \pm 0.3\%$) and much smaller than
 451 for the bed sediment sample ($72.2 \pm 10\%$). The inferred OC_{petro} concentration in the sediment is remarkably uniform
 452 in the cross-section, representing 0.04% of SPM (Figure 7b). This result is consistent with the OC contents of
 453 midstream sedimentary rocks at $0.09 \pm 0.08\%$ (Qu et al., 2020). In addition, these findings imply that OC_{petro}
 454 concentration does not depend on particle size and confirm previous findings of OC_{petro} being present in a range of
 455 clastic particles or as discrete particles (Galy et al., 2008a; Bouchez et al., 2014). In other words, the rock-derived OC
 456 has a relatively invariant contribution with depth (Galy et al., 2008a; Bouchez et al., 2014), meaning that biospheric
 457 OC exerts a first-order control on POC content and isotopic variations throughout the cross-section.

458 **Table 2: Summary of $\delta^{13}C$ and $\Delta^{14}C$ of source end members for POC in the Huanghe.**

End member	$\delta^{13}C$	$\Delta^{14}C$
OC_{ts}	$-24.8 \pm 1.9\%$	$-90 \pm 130\%$
OC_{lps}	$-22.7 \pm 1.0\%$	$-610 \pm 390\%$
OC_{petro}	$-28.1 \pm 1.5\%$	-1000%

459 At the study cross-section, OC_{ts} and OC_{lps} contribute 46.6%-55.4% and 34.5%-39.5% to the total POC, respectively
 460 (Figure 7a). The sum of these two components can be considered as OC_{bio} , which is $88.0 \pm 1.3\%$. The corresponding

461 OC_{bio} content of sediment is quite variable, ranging from 0.25% (sample JB 2-3) to 0.40% (sample JB 1-2), and
 462 generally decreases from the river surface to the bottom. Given the rather invariant OC_{petro} concentration in the
 463 sediment, there are thus marked heterogeneities of POC provenance in the cross-section. For instance, POC
 464 transported close to the right bank and in the finer SPM samples show a higher contribution from OC_{bio}. From the
 465 knowledge of the relative contributions of OC_{ts} and OC_{lps} and their corresponding ¹⁴C activity, the Fm values for the
 466 bulk OC_{bio} can be estimated based on mass balance. The modeled radiocarbon activity of OC_{bio} varies from 0.64 to
 467 0.75, corresponding to 3,570 to 2,300 ¹⁴C yrs. In summary, our results support the first-order control of OC_{bio}
 468 abundance on POC content and age in the Huanghe.



469 **Figure 7: (a) Relative contributions of the three different sources of Huanghe POC, (b) fractional OC weight percentage**
 470 **Huanghe POC at the Luokou cross-section, as inferred from a mixing model. OC_{ts} is the topsoil-derived OC, OC_{lps}**
 471 **represents the loess-paleosol sequence OC excluding topsoil, and OC_{petro} is the rock-derived OC eroded from the Huanghe**
 472 **middle reaches.**
 473

474 Applying the same mixing model to previously published Huanghe POC data (2011-2016, Table S1) shows (1)
 475 dominance of the OC_{bio} contribution to POC, (2) variable relative mixing proportions of OC_{ts} and OC_{lps}; (3) a wide
 476 range of ¹⁴C age for OC_{bio} (from 1,779 to 8,325 yrs). In particular, OC_{ts} and OC_{lps} contributed 28%-35% and 53%-
 477 63% to POC collected in 2013 (Hu et al., 2015), leading to 75-89% of OC_{bio}. Yu et al. (2019a) estimated that OC_{bio}
 478 contributed 63%-81% to the lower Huanghe POC (2015-2016) using a different mixing model. Using their data in our
 479 mixing model results in a higher OC_{bio} contribution of 88%-91%, consisting of 43%-55% for OC_{ts} and 36%-46% for
 480 OC_{lps}. The small difference in source contribution mainly results from the fact that old OC_{bio} from loess-paleosol

481 sequences was not considered in Yu et al. (2019a), and from the different isotopic signatures chosen for the POC
482 endmembers. However, both estimates ignore the possible presence of rock-derived OC in soils. In any case, our
483 results suggest that the Huanghe transports more OC_{bio}-derived POC than previously thought, with more aged, soil-
484 derived OC.

485 It is worth noticing that these calculations suggest that the OC_{lps} fraction in the Huanghe was significantly higher in
486 2013 than in 2016. As most Huanghe sediments are derived from the CLP, higher physical erosion in the CLP should
487 enhance supply of aged, refractory OC_{bio} to the river system. Consequently, the decrease in sediment supply from the
488 CLP initiated a few decades ago (Wang and Fu et al., 2016), which is likely to continue in the future, will probably
489 lead to the reduction of the contribution of OC_{lps} to total POC export from the Huanghe. This might have an impact
490 on the burial efficiency of riverine POC on the continental margins, as OC_{ts} is more labile than OC_{lps}, and thus more
491 prone to the remineralization process before burial. Moreover, decreasing erosion rate in the Huanghe basin will lead
492 to decreasing sediment accumulation rate in the estuary, which potentially favors the oxidation of all POC components
493 before burial (Blair and Aller, 2012). The time scale over which such effect could take place is yet unknown, as
494 anthropogenic intervention is the primary reason for the sediment yield reduction, through afforestation and soil and
495 water conservation measures in the CLP and reservoir operation in the middle reaches of the Huanghe. However, it is
496 plausible that in response to decreased terrestrial physical erosion on the Loess Plateau over at least decadal timescales,
497 an increased proportion of Huanghe POC will be oxidized before burial in the ocean, thereby leading to a weakened
498 preservation efficiency for the terrestrial eroded POC.

499 **5.3 POC export by the Huanghe**

500 In the Huanghe, POC content varies both vertically and laterally throughout the cross-section (Figure 2). This spatial
501 variability of both physical and chemical SPM characteristics must be considered when estimating integrated
502 instantaneous POC concentration and flux (Section 3.4).

503 We calculate that (Text S1) at the sampling time (July 2016), the Huanghe at Luokou transported 1,075 kg/s of SPM
504 for a water discharge of 731 m³/s, such that the spatially-integrated SPM concentration over the cross section (SPM_{int})
505 was 1,472 mg/L, a value relatively close to the straightforward average concentration of our 10 samples (1,286 mg/L).
506 The Luokou gauging station records a monthly SPM load of 1,826 kg/s in July 2016, and the daily average SPM load
507 of 1,096 kg/s for a daily average water discharge of 643 m³/s on the 16th and 17th of July 2016 (method: three water
508 samples collected at 0.5 m below the channel surface across the transect profile, data available at
509 <http://www.yrcc.gov.cn>). Even though the latter estimate neglects the vertical heterogeneity within this relatively
510 shallow river (< 5.0 m), estimates give similar results.

511 We further obtain an instantaneous POC flux of 3.69 kg/s, corresponding to a cross-section integrated average POC
512 content (POC_{int}%) of 0.34% when dividing this instantaneous POC flux by the instantaneous SPM load. Given the
513 relatively homogenous distribution of OC_{petro}, the instantaneous flux of OC_{petro} was calculated by multiplying the
514 average OC_{petro} content by the instantaneous cross-section integrated SPM flux, yielding 0.44 ± 0.18 kg/s. The
515 instantaneous OC_{bio} flux was then calculated by subtracting the instantaneous flux of OC_{petro} from the instantaneous
516 POC flux, yielding 3.25 ± 0.20 kg/s. Assuming that our SPM samples are representative in terms of POC content

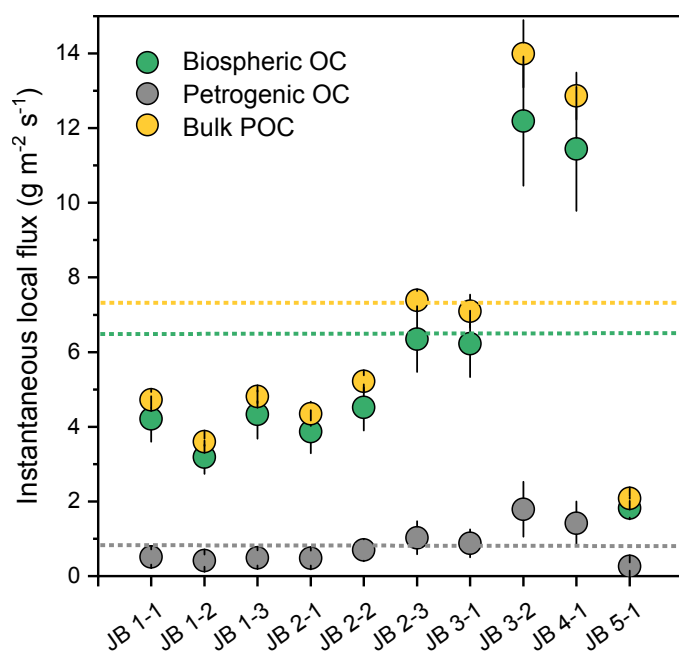
517 exported in July 2016, and taking the SPM flux of the gauging station for July, then the estimated fluxes of POC,
518 OC_{bio}, and OC_{petro} for the flood period of July 2016 are 6.1, 5.4, and 0.7 kg/s, respectively. Taking POC_{int} content for
519 estimating the annual POC flux yields a value of 1.1 kg/s consisting of 1.0 and 0.1 kg/s for OC_{bio} and OC_{petro} fluxes,
520 respectively. Note that these numbers are lower-bound estimates because POC content in Huanghe SPM collected
521 during flood periods is generally the lowest (Ran et al., 2013). Taking the highest POC content 0.75% reported in the
522 lower Huanghe in 2016 (Yu et al., 2019a), the estimated annual POC flux is 2.4 kg/s.

523 The above numbers present a sharp decrease compared to the estimated POC and OC_{bio} fluxes transported by the
524 Huanghe over the period 2008 to 2013. Galy et al. (2015) estimated an OC_{petro} flux of 1.9 kg/s and an OC_{bio} flux of
525 11.4 kg/s from 2008 to 2012 (SPM flux: 3,655 kg/s, YRCC 2016), while Tao et al. (2018) reported an OC_{petro} flux of
526 5.8 kg/s and a similar OC_{bio} flux of 12.6 kg/s from June 2012 to May 2013 (SPM flux: 5,723 kg/s, YRCC 2016).

527 We first note that previous estimates of POC flux in the Huanghe might be biased as these estimates neglect the
528 variability over the cross-section (*e.g.*, Hu et al., 2015; Ran et al., 2013; Tao et al., 2015), SPM samples analyzed so
529 far for the Huanghe were generally collected within the first 0.5 m below the surface, meaning that previous POC
530 estimates did not consider the observed vertical and lateral POC heterogeneities and have thus misestimated POC
531 sources and fluxes. Those estimates were calculated by multiplying an individual surface POC content by the
532 corresponding monthly or weekly suspended sediment load, as provided by hydrological stations. Such estimates can
533 be problematic because POC content in SPM generally decreases from top to bottom (Figure 2), resulting in biased
534 surface-based estimates of fluxes (Bouchez et al., 2014). Using our cross-section data, we can estimate the bias in
535 POC flux estimates when a single sample is used for such flux estimates, by multiplying depth-integrated sediment
536 flux by the POC content of each sample. Such calculation shows different POC fluxes ranging from -15% to +30%
537 compared to the depth-integrated estimate, which is mostly influenced by the variable POC content. Considering SPM
538 collected at the channel surface, POC flux estimates using samples JB 1-1 and JB 2-1 are 28% and 15% higher,
539 respectively, and are 6% and 5% lower using samples JB 3-1 and JB 5-1, respectively, than the depth-integrated
540 estimate. This simple sensitivity analysis shows that channel surface sampling of SPM alone does not necessarily
541 result in an overestimation of POC flux because of lateral heterogeneity, even though the POC content of SPM is
542 generally higher at the surface than at the bottom (Figure 2). Consequently, and although accurate estimation of POC
543 fluxes requires grain-size variations to be accounted for, the corresponding bias cannot explain the large difference
544 between our estimates of Huanghe POC export for the year 2016 and previous estimates for preceding years. The SPM
545 flux is 336 kg/s in 2016 and 762 kg/s over the period 2014 to 2016, which is one order of magnitude lower than values
546 reported from 2008 to 2013 (YRCC 2016). The dramatic decrease in sediment load of the Huanghe (Wang and Fu et
547 al., 2016) has most likely exerted a first-order control on the reduction in POC export from the Huanghe river system,
548 and will probably continue to do so in the near future.

549 In the lower Huanghe, the POC content is very low and has small variance among different size fractions (Get et al.,
550 2020), such that the POC flux is controlled by the SPM flux. In particular, it is worth noting that the Huanghe displays
551 strong density stratification effects compared to other rivers (Moodie et al., 2022), with near-bed flow dominating the
552 transport of SPM. In order to appraise how spatial and temporal variability in SPM flux could influence POC export,
553 "local" POC loads can be calculated throughout the cross-section using the local water velocity, SPM concentration,

554 and POC content (Figure 8). In general, in the lower Huanghe more POC is transported near the riverbed and above
 555 shallower bathymetry on the left side of the channel (except for profile JB 5). For instance, there is a nearly two-fold
 556 increase in POC export from the surface to the bottom for the JB 2 and JB 3 profiles. The maximum local bulk POC
 557 ($14.0 \text{ gC m}^{-2} \text{ s}^{-1}$), OC_{bio} ($12.2 \text{ gC m}^{-2} \text{ s}^{-1}$), and OC_{petro} export ($1.8 \text{ gC m}^{-2} \text{ s}^{-1}$) are of sample JB 3-2, representing over
 558 6 times the size of the corresponding minimum value (sample JB 5-1). This spatial pattern of POC load is almost the
 559 reverse of the POC% variation over the cross-section, again stressing the importance of sediment river dynamics in
 560 POC delivery. From these considerations, it could be anticipated that during the low-water season, when water velocity
 561 is slower, near-bottom Huanghe SPM is deposited on the channel bed, withdrawing a significant fraction of the POC
 562 export, as shown in other large rivers (Ke et al., 2022). This topic should be further examined in future research, in
 563 order to systematically investigate the stratification of sediment and associated OC transport dynamics in lowland and
 564 high-turbidity fluvial systems.



565 **Figure 8: Estimates of instantaneous “local” fluxes of Huanghe bulk POC, OC_{bio} and OC_{petro} , calculated for each sample of**
 566 **the Luokou cross-section. The three dotted lines marked in orange, green, and grey represent the corresponding**
 567 **instantaneous, cross-section integrated fluxes. The error bar represents 1 standard deviation.**

569 Interestingly, anthropogenic activities may have antagonistic effects on POC export. Deforestation, agriculture, and
 570 mining have considerably enhanced the sediment yield from the CLP since the mid-Holocene (He et al., 2006) while
 571 the construction of large dams, soil and water conservation measures, and afforestation has considerably reduced the
 572 sediment yield since the 1950s (Wang and Fu et al., 2016; Wang et al., 2007; Syvitski et al., 2005). Yet the Huanghe
 573 exports substantial OC_{bio} and OC_{petro} with a significantly higher burial efficiency (avg. ca. 42%; Sun et al., 2018) than
 574 other large fluvial systems entering passive continental margins, such as the Changjiang, Amazon, and Mississippi
 575 (Blair and Aller, 2012). It is reported that aged soil OC is nearly fully preserved in continental margins and that OC_{petro}
 576 has a ca. 70% burial efficiency (Tao et al., 2016). However, the contribution of the Huanghe OC burial to the global
 577 C sink is likely to be lower in the future as the consequence of 1) sharp decrease in SPM and POC export due to

578 weakened physical erosion in the CLP; 2) reduced sediment accumulation rate favoring OC remineralization in
579 estuaries (Blair and Aller, 2012; Walling and Fan, 2003; Milliman and Farnsworth, 2011; Galy et al., 2015).

580 **6 Conclusions**

581 In this contribution, we present the first detailed study of particulate organic carbon (POC) over a complete river cross-
582 section of the Huanghe, providing new perspectives on the transport mode, source, and instantaneous fluxes of POC
583 in this highly turbid large river.

584 At the scale of a cross-section, physical and chemical properties of SPM are heterogeneous both vertically and
585 laterally, a feature that is mainly controlled by bathymetry and hydrodynamic sorting. Resuspension of bed sediment
586 and local erosion of the right bank together impact the suspended POC composition at the sampled location. This
587 spatial heterogeneity shows that near-bottom SPM plays a dominant role in the delivery of OC_{bio} (topsoil and deep
588 soil OC combined) and OC_{petro}. Despite a relatively shallow river channel (< 5.0 m) and narrow width (< 200 m), we
589 show how the heterogeneity of POC transport over a cross-section needs to be considered in constraining POC
590 transport mode and estimating POC fluxes.

591 Despite its millennial age, POC in the Huanghe is dominated by OC_{bio} with a contribution of 88.0 ± 1.3 %. OC_{petro}
592 content in SPM is relatively homogeneous (0.04% - 0.05%) over the cross-section, indicating that the variability in
593 bulk POC age is mainly controlled by the variability in OC_{bio} content, especially in the finest SPM fraction. OC_{bio} ages
594 deduced from the application of a mixing model to previously published data (record period 2011-2016) are highly
595 variable, ranging from 1,779 to 8,325 ¹⁴C yrs. We interpret this feature as resulting from the erosion of deep horizons
596 by gully systems in the loess-paleosol sequences containing ¹⁴C-dead OC_{bio}. Enhanced erosion of deep loess-paleosol
597 horizons mobilizes aged and refractory OC to the ocean, with high burial efficiency on the passive margin. The erosion
598 of loess-paleosol horizons is thus an efficient process of CO₂ burial. However, the construction of large dams has
599 drastically affected the sediment load of the Huanghe system and retains substantial quantities of sediments that were
600 previously exported to the ocean. Future work is needed to further quantify how these anthropogenic modifications
601 alter POC composition and transport, by conducting comprehensive cross-section sampling campaigns over extended
602 time series upstream and downstream from dams.

603 **Appendix A**

604 Fluvial POC delivered in the Huanghe POC could originate from three terrestrial sources (Table. 2). As topsoil
605 typically contains recently photosynthesized OC_{bio}, we used a $\delta^{13}\text{C}$ value of $-24.8 \pm 1.9\text{‰}$ (n=166) according to the
606 subsurface soil OC values measured across the Huanghe basin (Rao et al., 2017). Over the sampled cross-section, the
607 depleted ¹³C values indicate the dominant and almost exclusive input of C3 plant-derived material to the Huanghe
608 POC in the lower reaches. Based on ¹⁴C (Liu et al., 2012) and ¹⁰Be (Zhou et al., 2010) dating of < 10 cm-deep soil
609 horizons in the Huanghe Basin, the average age of topsoil was chosen as being younger than 2,000 yrs (*i.e.*, $\Delta^{14}\text{C} >$
610 -220‰). As for the topsoil end member includes modern biospheric material ($\Delta^{14}\text{C}$ around 40‰, Hua et al., 2013),
611 we assigned a $\Delta^{14}\text{C}$ value of $-90 \pm 130\text{‰}$ (Fm = 0.91 ± 0.13). This range also includes the range of $\Delta^{14}\text{C}$ values of

612 pre-aged soil OC indicated by the long-chain n-C₂₄₊₂₆₊₂₈ alkanols of the Huanghe POC reported by Tao et al. (2015)
613 and Yu et al. (2019a). Their results show consistent POC $\Delta^{14}\text{C}$ values in the lower reaches of $-204 \pm 20\text{‰}$ ($F_m = 0.80$
614 ± 0.03 , $n=7$) from June 2015 to May 2016 and $-219 \pm 33\text{‰}$ ($F_m = 0.79 \pm 0.04$, $n=4$) at Kenli and of $-198 \pm 15\text{‰}$ (F_m
615 $= 0.81 \pm 0.02$, $n=6$) from June 2015 to April 2016 at Huayuankou (Tao et al., 2015; Yu et al., 2019a).

616 The second end member should be characterized by aged and refractory OC from the loess-paleosol sequence
617 excluding topsoil (upper 10 m) of the CLP. Radiocarbon dating has an upper age limit of around 50,000 yrs, age above
618 which F_m is equal to 0. However, radiocarbon-free OC spanning from 50,000 to 100,000 yrs must still be considered
619 as OC_{bio} in the long-term carbon cycle. Here, we name this ignored OC as the “dormant” OC, without which the OC_{bio}
620 (*i.e.*, less than 100,000 yrs old) would be underestimated to some extent because the radiocarbon-free OC would be
621 misinterpreted as having a petrogenic origin. To consider this “dormant” OC, a $\delta^{13}\text{C}$ values of $-22.7 \pm 1.0\text{‰}$ ($n=34$,
622 Ning et al., 2006) and a $\Delta^{14}\text{C}$ values of $-610 \pm 390\text{‰}$ ($F_m, 0.39 \pm 0.39$) were adopted based on an average of values
623 over the whole loess-paleosol sequence. Although radiocarbon-free (*i.e.*, older than 100,000 yrs) OC overlaps with
624 this end member, such old soil organic carbon is probably not mobilized as modern gully erosion mainly concerns the
625 upper 10 m of the loess-paleosol sequences, where soil OC_{bio} is assumed to be significantly younger comparatively
626 (Figure 5).

627 Rock-derived OC from the QTP and the CLP, as well as kerogen from oil-gas fields from the Ordos Basin,
628 were all considered to be possible contributors to the OC_{petro} endmember. The $\delta^{13}\text{C}$ of OC_{petro} greatly varies between
629 the QTP ($-21.2 \pm 1.2\text{‰}$, $n=11$, Liu et al., 2007) and the CLP ($-26.8 \pm 0.5\text{‰}$, $n=8$, Qu et al., 2020). However, most of
630 the sediments eroded from the QTP are not transferred to the lower reaches as they remain trapped in the CLP and the
631 western Mu Us desert (Nie et al., 2015; Licht et al., 2016; Pan et al., 2016). In addition, the construction of large dams
632 in the upper reaches has considerably reduced the transfer of solid materials downstream (Wang et al., 2007).
633 Therefore, rock-derived OC inherited from the denudation of the QTP region is not further considered. Kerogen from
634 the oil-gas fields of the Ordos Basin in the CLP region (Figure 1) has $\delta^{13}\text{C}$ values of $-29.2 \pm 0.9\text{‰}$ ($n=10$, Guo et al.,
635 2014). Taking these constraints together, we consider a $\delta^{13}\text{C}$ value of $-28.1 \pm 1.5\text{‰}$ ($n=18$) for the OC_{petro} end member,
636 and a $\Delta^{14}\text{C}$ value of -1000‰ ($F_m = 0$) by definition.

637 Key Points

- 638 Bank erosion in lower Huanghe provides recent organic carbon to fluvial transport, altering the particulate
639 organic carbon transport over a river channel cross-section;
- 640 Erosion of deep soil horizons of the loess-paleosol sequence contributes radiocarbon-dead organic carbon
641 from the biosphere to the Huanghe;
- 642 Channel-bottom transport in the Huanghe is the primary process of exporting fluvial particulate organic
643 carbon to the estuary.

644 Data availability

645 All datasets are included in the paper and the supplementary materials.

646 **Author contributions**

647 DC, JB, CQ, and YK conceptualized the study. DC, JB, YK, MM, and BC determined the methodology. HC and JC
648 collected the sediment samples. YK, MM, and AN assisted with elemental and isotopic carbon analysis. DC and CQ
649 supervised the work. KY performed data analysis and wrote the original draft, and all authors contributed to the review
650 and editing of the paper.

651 **Competing interests**

652 We declare there is no competing interest.

653 **Acknowledgments**

654 We thank Yulong Liu and Shengliu Yuan for their help during sampling and filtering. We also thank François Thil
655 and Nadine Tissenerat for invaluable help when running the ECHoMICADAS, and Pierre Barré for use of the
656 Beckman Coulter's LS 13 320 for particle size analysis at École normale supérieure.

657 **Financial support**

658 This study was financially supported by the Agence Nationale de la Recherche (ANR) SEDIMAN (Grant ANR-15-
659 CE01-0012), the National Natural Science Foundation of China (NSFC), grants 41561134017, 41625012, and the
660 China Scholarship Council (CSC) to Yutian Ke (No.201706180008).

661 **References**

- 662 Baronas, J. J., Stevenson, E. I., Hackney, C. R., Darby, S. E., Bickle, M. J., Hilton, R. G., Larkin, C. S., Parsons, D.
663 R., Myo Khaing, A., and Tipper, E. T.: Integrating Suspended Sediment Flux in Large Alluvial River Channels:
664 Application of a Synoptic Rouse-Based Model to the Irrawaddy and Salween Rivers, *Journal of Geophysical Research:*
665 *Earth Surface*, 125, <https://doi.org/10.1029/2020jf005554>, 2020.
- 666 Bianchi, T. S.: The role of terrestrially derived organic carbon in the coastal ocean: A changing paradigm and the
667 priming effect, *Proceedings of the National Academy of Sciences*, 108, 19473–19481,
668 <https://doi.org/10.1073/pnas.1017982108>, 2011.
- 669 Bird, A., Stevens, T., Rittner, M., Vermeesch, P., Carter, A., Andò, S., Garzanti, E., Lu, H., Nie, J., Zeng, L., Zhang,
670 H., and Xu, Z.: Quaternary dust source variation across the Chinese Loess Plateau, *Palaeogeography,*
671 *Palaeoclimatology, Palaeoecology*, 435, 254–264, <https://doi.org/10.1016/j.palaeo.2015.06.024>, 2015.
- 672 Blair, N. E. and Aller, R. C.: The Fate of Terrestrial Organic Carbon in the Marine Environment, *Annual Review of*
673 *Marine Science*, 4, 401–423, <https://doi.org/10.1146/annurev-marine-120709-142717>, 2012.
- 674 Blair, N. E., Leithold, E. L., Brackley, H., Trustrum, N., Page, M., and Childress, L.: Terrestrial sources and export of
675 particulate organic carbon in the Waipaoa sedimentary system: Problems, progress and processes, *Marine Geology*,
676 270, 108–118, <https://doi.org/10.1016/j.margeo.2009.10.016>, 2010.
- 677 Bouchez, J., Galy, V., Hilton, R. G., Gaillardet, J., Moreira-Turcq, P., Pérez, M. A., France-Lanord, C., and Maurice,
678 L.: Source, transport and fluxes of Amazon River particulate organic carbon: Insights from river sediment depth-
679 profiles, *Geochimica et Cosmochimica Acta*, 133, 280–298, <https://doi.org/10.1016/j.gca.2014.02.032>, 2014.
- 680 Bouchez, J., Gaillardet, J., France-Lanord, C., Maurice, L., and Dutra-Maia, P.: Grain size control of river suspended
681 sediment geochemistry: Clues from Amazon River depth profiles, *Geochemistry, Geophysics, Geosystems*, 12, n/a-
682 n/a, <https://doi.org/10.1029/2010gc003380>, 2011a.

683 Bouchez, J., Lupker, M., Gaillardet, J., France-Lanord, C., and Maurice, L.: How important is it to integrate riverine
684 suspended sediment chemical composition with depth? Clues from Amazon River depth-profiles, *Geochimica et*
685 *Cosmochimica Acta*, 75, 6955–6970, <https://doi.org/10.1016/j.gca.2011.08.038>, 2011.

686 Carignan, J., Hild, P., Mevelle, G., Morel, J., and Yeghicheyan, D.: Routine Analyses of Trace Elements in Geological
687 Samples using Flow Injection and Low Pressure On-Line Liquid Chromatography Coupled to ICP-MS: A Study of
688 Geochemical Reference Materials BR, DR-N, UB-N, AN-G and GH, *Geostandards Newsletter*, 25, 187–198,
689 <https://doi.org/10.1111/j.1751-908X.2001.tb00595.x>, 2001.

690 Cauwet, G. and Mackenzie, F. T.: Carbon inputs and distribution in estuaries of turbid rivers: the Yang Tze and Yellow
691 rivers (China), *Marine Chemistry*, 43, 235–246, [https://doi.org/10.1016/0304-4203\(93\)90229-h](https://doi.org/10.1016/0304-4203(93)90229-h), 1993.

692 Cheng, P., Burr, G. S., Zhou, W., Chen, N., Hou, Y., Du, H., Fu, Y., and Lu, X.: The deficiency of organic matter 14C
693 dating in Chinese Loess-paleosol sample, *Quaternary Geochronology*, 56, 101051,
694 <https://doi.org/10.1016/j.quageo.2019.101051>, 2020.

695 Curry, K. J., Bennett, R. H., Mayer, L. M., Curry, A., Abril, M., Biesiot, P. M., and Hulbert, M. H.: Direct visualization
696 of clay microfabric signatures driving organic matter preservation in fine-grained sediment, *Geochimica et*
697 *Cosmochimica Acta*, 71, 1709–1720, <https://doi.org/10.1016/j.gca.2007.01.009>, 2007.

698 Dellinger, M., Gaillardet, J., Bouchez, J., Calmels, D., Galy, V., Hilton, R. G., Louvat, P., and France-Lanord, C.:
699 Lithium isotopes in large rivers reveal the cannibalistic nature of modern continental weathering and erosion, *Earth*
700 *and Planetary Science Letters*, 401, 359–372, <https://doi.org/10.1016/j.epsl.2014.05.061>, 2014.

701 Feng, X., Feakins, S. J., Liu, Z., Ponton, C., Wang, R. Z., Karkabi, E., Galy, V., Berelson, W. M., Nottingham, A.
702 T., Meir, P., and West, A. J.: Source to sink: Evolution of lignin composition in the Madre de Dios River system
703 with connection to the Amazon basin and offshore, *Journal of Geophysical Research: Biogeosciences*, 121, 1316–
704 1338, <https://doi.org/10.1002/2016JG003323>, 2016.

705 Freymond, C. V., Lupker, M., Peterse, F., Haghypour, N., Wacker, L., Filip, F., Giosan, L., and Eglinton, T. I.:
706 Constraining Instantaneous Fluxes and Integrated Compositions of Fluvially Discharged Organic Matter, *Geochem*
707 *Geophys Geosy*, 19, 2453–2462, <https://doi.org/10.1029/2018gc007539>, 2018.

708 Gaillardet, J., Dupré, B., Louvat, P., and Allègre, C. J.: Global silicate weathering and CO₂ consumption rates deduced
709 from the chemistry of large rivers, *Chemical Geology*, 159, 3–30, [https://doi.org/10.1016/s0009-2541\(99\)00031-5](https://doi.org/10.1016/s0009-2541(99)00031-5),
710 1999.

711 Galy, V. and Eglinton, T.: Protracted storage of biospheric carbon in the Ganges–Brahmaputra basin, *Nature Geosci*,
712 4, 843–847, <https://doi.org/10.1038/ngeo1293>, 2011.

713 Galy, V., Beyssac, O., France-Lanord, C., and Eglinton, T.: Recycling of graphite during Himalayan erosion: a
714 geological stabilization of carbon in the crust, *Science*, 322, 943–5, <https://doi.org/10.1126/science.1161408>, 2008a.

715 Galy, V., France-Lanord, C., and Lartiges, B.: Loading and fate of particulate organic carbon from the Himalaya to
716 the Ganga–Brahmaputra delta, *Geochimica et Cosmochimica Acta*, 72, 1767–1787,
717 <https://doi.org/10.1016/j.gca.2008.01.027>, 2008b.

718 Galy, V., France-Lanord, C., Beyssac, O., Faure, P., Kudrass, H., and Palhol, F.: Efficient organic carbon burial in the
719 Bengal fan sustained by the Himalayan erosional system, *Nature*, 450, 407–10, <https://doi.org/10.1038/nature06273>,
720 2007.

721 Galy, V., Peucker-Ehrenbrink, B., and Eglinton, T.: Global carbon export from the terrestrial biosphere controlled by
722 erosion, *Nature*, 521, 204–7, <https://doi.org/10.1038/nature14400>, 2015.

723 Garzanti, E., Andò, S., France-Lanord, C., Vezzoli, G., Censi, P., Galy, V., and Najman, Y.: Mineralogical and
724 chemical variability of fluvial sediments: 1. Bedload sand (Ganga–Brahmaputra, Bangladesh), *Earth and Planetary*
725 *Science Letters*, 299, 368–381, <https://doi.org/10.1016/j.epsl.2010.09.017>, 2010.

726 Garcia, M.: *Sedimentation Engineering*, American Society of Civil Engineers, (pp. 21-163)
727 <https://doi.org/10.1061/9780784408148>, 2008.

728 Ge, T., Xue, Y., Jiang, X., Zou, L., and Wang, X.: Sources and radiocarbon ages of organic carbon in different grain
729 size fractions of Yellow River-transported particles and coastal sediments, *Chemical Geology*, 534, 119452,
730 <https://doi.org/10.1016/j.chemgeo.2019.119452>, 2020.

731 Gu, Z., Duan, X., Shi, Y., Li, Y., and Pan, X.: Spatiotemporal variation in vegetation coverage and its response to
732 climatic factors in the Red River Basin, China, *Ecological Indicators*, 93, 54–64,
733 <https://doi.org/10.1016/j.ecolind.2018.04.033>, 2018.

734 Guo, H., Jia, W., Peng, P., Lei, Y., Luo, X., Cheng, M., Wang, X., Zhang, L., and Jiang, C.: The composition and its
735 impact on the methane sorption of lacustrine shales from the Upper Triassic Yanchang Formation, Ordos Basin, China,
736 *Marine and Petroleum Geology*, 57, 509–520, <https://doi.org/10.1016/j.marpetgeo.2014.05.010>, 2014.

737 Guo, K., Zou, T., Jiang, D., Tang, C., and Zhang, H.: Variability of Yellow River turbid plume detected with satellite
738 remote sensing during water-sediment regulation, *Continental Shelf Research*, 135, 74–85,
739 <https://doi.org/10.1016/j.csr.2017.01.017>, 2017.

740 Guo, L., Ping, C.-L., and Macdonald, R. W.: Mobilization pathways of organic carbon from permafrost to arctic rivers
741 in a changing climate, *Geophysical Research Letters*, 34, <https://doi.org/10.1029/2007GL030689>, 2007.

742 Guo, Z. T., Ruddiman, W. F., Hao, Q. Z., Wu, H. B., Qiao, Y. S., Zhu, R. X., Peng, S. Z., Wei, J. J., Yuan, B. Y., and
743 Liu, T. S.: Onset of Asian desertification by 22 Myr ago inferred from loess deposits in China, *Nature*, 416, 159–163,
744 <https://doi.org/10.1038/416159a>, 2002.

745 Hatté, C., Arnold, M., Dapoigny, A., Daux, V., Delibrias, G., Boisguezeneuc, D. D., Fontugne, M., Gauthier, C.,
746 Guillier, M.-T., Jacob, J., Jaudon, M., Kaltnecker, É., Labeyrie, J., Noury, C., Paterne, M., Pierre, M., Phouybanhdyt,
747 B., Poupeau, J.-J., Tannau, J.-F., Thil, F., Tisnérat-Laborde, N., and Valladas, H.: Radiocarbon dating on
748 ECHOMICADAS, LSCE, Gif-Sur-Yvette, France: new and updated chemical procedures, *Radiocarbon*, 1–16,
749 <https://doi.org/10.1017/RDC.2023.46>, 2023.

750 He, X., Zhou, J., Zhang, X., and Tang, K.: Soil erosion response to climatic change and human activity during the
751 Quaternary on the Loess Plateau, China, *Reg Environ Change*, 6, 62–70, <https://doi.org/10.1007/s10113-005-0004-7>,
752 2006.

753 Hemingway, J. D., Hilton, R. G., Hovius, N., Eglinton, T. I., Haghypour, N., Wacker, L., Chen, M. C., and Galy, V.
754 V.: Microbial oxidation of lithospheric organic carbon in rapidly eroding tropical mountain soils, *Science*, 360, 209–
755 212, <https://doi.org/10.1126/science.aao6463>, 2018.

756 Hemingway, J. D., Rothman, D. H., Grant, K. E., Rosengard, S. Z., Eglinton, T. I., Derry, L. A., and Galy, V. V.:
757 Mineral protection regulates long-term global preservation of natural organic carbon, *Nature*, 570, 228–231,
758 <https://doi.org/10.1038/s41586-019-1280-6>, 2019.

759 Hilton, R. G., Gaillardet, J., Calmels, D., and Birck, J.-L.: Geological respiration of a mountain belt revealed by the
760 trace element rhenium, *Earth and Planetary Science Letters*, 403, 27–36, <https://doi.org/10.1016/j.epsl.2014.06.021>,
761 2014.

762 Hilton, R. G., Galy, A., Hovius, N., Horng, M.-J., and Chen, H.: Efficient transport of fossil organic carbon to the
763 ocean by steep mountain rivers: An orogenic carbon sequestration mechanism, *Geology*, 39, 71–74,
764 <https://doi.org/10.1130/g31352.1>, 2011.

765 Hilton, R. G., Galy, V., Gaillardet, J., Dellinger, M., Bryant, C., O'Regan, M., Grocke, D. R., Coxall, H., Bouchez, J.,
766 and Calmels, D.: Erosion of organic carbon in the Arctic as a geological carbon dioxide sink, *Nature*, 524, 84–7,
767 <https://doi.org/10.1038/nature14653>, 2015.

768 Hu, B., Li, J., Bi, N., Wang, H., Wei, H., Zhao, J., Xie, L., Zou, L., Cui, R., Li, S., Liu, M., and Li, G.: Effect of
769 human-controlled hydrological regime on the source, transport, and flux of particulate organic carbon from the lower
770 Huanghe (Yellow River), *Earth Surface Processes and Landforms*, 40, 1029–1042, <https://doi.org/10.1002/esp.3702>,
771 2015.

772 Hua, Q., Barbetti, M., and Rakowski, A. Z.: Atmospheric Radiocarbon for the Period 1950–2010, *Radiocarbon*, 55,
773 2059–2072, https://doi.org/10.2458/azu_js_rc.v55i2.16177, 2013.

774 Huang, C. C., and Ren, Z: Fluvial erosion and the formation of gully systems over the Chinese Loess Plateau, *WSEAS*
775 *Transactions on Environment and Development*, 2(2), 141-145, 2006.

776 Jahn, B., Gallet, S., and Han, J.: Geochemistry of the Xining, Xifeng and Jixian sections, Loess Plateau of China:
777 eolian dust provenance and paleosol evolution during the last 140 ka, *Chemical Geology*, 178, 71–94,
778 [https://doi.org/10.1016/S0009-2541\(00\)00430-7](https://doi.org/10.1016/S0009-2541(00)00430-7), 2001.

779 Ke, Y., Calmels, D., Bouchez, J., and Quantin, C.: MODern River archivEs of Particulate Organic Carbon:
780 MOREPOC, *Earth System Science Data Discussions*, 1–19, <https://doi.org/10.5194/essd-2022-161>, 2022.

781 Keil, R. G., Mayer, L. M., Quay, P. D., Richey, J. E., and Hedges, J. I.: Loss of organic matter from riverine particles
782 in deltas, *Geochimica et Cosmochimica Acta*, 61, 1507–1511, [https://doi.org/10.1016/S0016-7037\(97\)00044-6](https://doi.org/10.1016/S0016-7037(97)00044-6), 1997.

783 Gen Li, X. T. W., Zhongfang Yang, Changping Mao, A. Joshua West, Junfeng Ji: Dam-triggered organic carbon
784 sequestration makes the Changjiang (Yangtze) river basin (China) a significant carbon sink, *Journal of Geophysical*
785 *Research: Biogeosciences*, 2015.

786 Li, P., Chen, J., Zhao, G., Holden, J., Liu, B., Chan, F. K. S., Hu, J., Wu, P., and Mu, X.: Determining the drivers and
787 rates of soil erosion on the Loess Plateau since 1901, *Science of The Total Environment*, 823, 153674,
788 <https://doi.org/10.1016/j.scitotenv.2022.153674>, 2022.

789 Licht, A., Pullen, A., Kapp, P., Abell, J., and Giesler, N.: Eolian cannibalism: Reworked loess and fluvial sediment as
790 the main sources of the Chinese Loess Plateau, *GSA Bulletin*, 128, 944–956, <https://doi.org/10.1130/B31375.1>, 2016.

791 Liu, G., Xu, W., Zhang, Q., & Xia, Z. : Holocene Soil Chronofunctions, Luochuan, Chinese Loess Plateau.
792 *Radiometric Dating*, 41, 2012.

793 Liu, J. and Liu, W.: Soil nitrogen isotopic composition of the Xifeng loess-paleosol sequence and its potential for use
794 as a paleoenvironmental proxy, *Quaternary International*, 440, 35–41, <https://doi.org/10.1016/j.quaint.2016.04.018>,
795 2017.

796 Liu, W., Yang, H., Ning, Y., and An, Z.: Contribution of inherent organic carbon to the bulk $\delta^{13}\text{C}$ signal in loess
797 deposits from the arid western Chinese Loess Plateau, *Organic Geochemistry*, 38, 1571–1579,
798 <https://doi.org/10.1016/j.orggeochem.2007.05.004>, 2007.

799 Ludwig, W., Probst, J.-L., and Kempe, S.: Predicting the oceanic input of organic carbon by continental erosion,
800 *Global Biogeochemical Cycles*, 10, 23–41, <https://doi.org/10.1029/95gb02925>, 1996.

801 Mayorga, E., Aufdenkampe, A. K., Masiello, C. A., Krusche, A. V., Hedges, J. I., Quay, P. D., Richey, J. E., and
802 Brown, T. A.: Young organic matter as a source of carbon dioxide outgassing from Amazonian rivers, *Nature*, 436,
803 538–41, <https://doi.org/10.1038/nature03880>, 2005.

804 Milliman, J. D. and Farnsworth, K. L.: *River discharge to the coastal ocean: a global synthesis*, Cambridge University
805 Press, 2011.

806 Milliman, J. D., Yun-Shan, Q., Mei-E, R., and Saito, Y.: Man's Influence on the Erosion and Transport of Sediment
807 by Asian Rivers: The Yellow River (Huanghe) Example, *The Journal of Geology*, 95, 751–762,
808 <https://doi.org/10.1086/629175>, 1987.

809 Moodie, A. J., Nittrouer, J. A., Ma, H., Carlson, B. N., Wang, Y., Lamb, M. P., and Parker, G.: Suspended Sediment-
810 Induced Stratification Inferred From Concentration and Velocity Profile Measurements in the Lower Yellow River,
811 China, *Water Resources Research*, 58, e2020WR027192, <https://doi.org/10.1029/2020WR027192>, 2022.

812 Moore, J. W., and Semmens, B. X.: Incorporating uncertainty and prior information into stable isotope mixing
813 models. *Ecology Letters*, 11(5), 470–480, <https://doi.org/10.1111/j.1461-0248.2008.01163.x>, 2008.

814 Ning, Y., Liu, W., and An, Z.: Variation of soil $\delta^{13}\text{C}$ values in Xifeng loess-paleosol sequence and its
815 paleoenvironmental implication, *Chinese Sci Bull*, 51, 1350–1354, <https://doi.org/10.1007/s11434-006-1350-7>, 2006.

816 Pan, B., Pang, H., Gao, H., Garzanti, E., Zou, Y., Liu, X., Li, F., and Jia, Y.: Heavy-mineral analysis and provenance
817 of Yellow River sediments around the China Loess Plateau, *Journal of Asian Earth Sciences*, 127, 1–11,
818 <https://doi.org/10.1016/j.jseaes.2016.06.006>, 2016.

819 Qu, Y., Jin, Z., Wang, J., Wang, Y., Xiao, J., Gou, L.-F., Zhang, F., Liu, C.-Y., Gao, Y., Suarez, M. B., and Xu, X.:
820 The sources and seasonal fluxes of particulate organic carbon in the Yellow River, *Earth Surface Processes and
821 Landforms*, <https://doi.org/10.1002/esp.4861>, 2020.

822 Ran, L., Lu, X. X., and Xin, Z.: Erosion-induced massive organic carbon burial and carbon emission in the Yellow
823 River basin, China, *Biogeosciences*, 11, 945–959, <https://doi.org/10.5194/bg-11-945-2014>, 2014.

824 Ran, L., Lu, X. X., Sun, H., Han, J., Li, R., and Zhang, J.: Spatial and seasonal variability of organic carbon transport
825 in the Yellow River, China, *Journal of Hydrology*, 498, 76–88, <https://doi.org/10.1016/j.jhydrol.2013.06.018>, 2013.

826 Rao, Z., Guo, W., Cao, J., Shi, F., Jiang, H., and Li, C.: Relationship between the stable carbon isotopic composition
827 of modern plants and surface soils and climate: A global review, *Earth-Science Reviews*, 165, 110–119,
828 <https://doi.org/10.1016/j.earscirev.2016.12.007>, 2017.

829 Repasch, M., Scheingross, J. S., Hovius, N., Lupker, M., Wittmann, H., Haghypour, N., Gröcke, D. R., Orfeo, O.,
830 Eglinton, T. I., and Sachse, D.: Fluvial organic carbon cycling regulated by sediment transit time and mineral
831 protection, *Nat. Geosci.*, 14, 842–848, <https://doi.org/10.1038/s41561-021-00845-7>, 2021.

832 Rouse, H.: Modern Conceptions of the Mechanics of Fluid Turbulence, *Transactions of the American Society of Civil
833 Engineers*, 102, 463–505, <https://doi.org/10.1061/TACEAT.0004872>, 1937.

834 Schwab, M. S., Hilton, R. G., Haghypour, N., Baronas, J. J., and Eglinton, T. I.: Vegetal Undercurrents—Obscured
835 Riverine Dynamics of Plant Debris, *Journal of Geophysical Research: Biogeosciences*, 127, e2021JG006726,
836 <https://doi.org/10.1029/2021JG006726>, 2022.

837 Shi, H. and Shao, M.: Soil and water loss from the Loess Plateau in China, *Journal of Arid Environments*, 45, 9–20,
838 <https://doi.org/10.1006/jare.1999.0618>, 2000.

839 Stevens, T., Carter, A., Watson, T. P., Vermeesch, P., Andò, S., Bird, A. F., Lu, H., Garzanti, E., Cottam, M. A., and
840 Sevastjanova, I.: Genetic linkage between the Yellow River, the Mu Us desert and the Chinese Loess Plateau,
841 *Quaternary Science Reviews*, 78, 355–368, <https://doi.org/10.1016/j.quascirev.2012.11.032>, 2013.

842 Stock BC and Semmens BX. 2016. MixSIAR GUI User Manual. Version
843 3.1. <https://github.com/brianstock/MixSIAR>. doi:10.5281/zenodo.1209993.

844 Sun, D., Tang, J., He, Y., Liao, W., and Sun, Y.: Sources, distributions, and burial efficiency of terrigenous organic
845 matter in surface sediments from the Yellow River mouth, northeast China, *Organic Geochemistry*, 118, 89–102,
846 <https://doi.org/10.1016/j.orggeochem.2017.12.009>, 2018.

847 Syvitski, J. P. M., Vörösmarty, C. J., Kettner, A. J., and Green, P.: Impact of Humans on the Flux of Terrestrial
848 Sediment to the Global Coastal Ocean, *Science*, 308, 376–380, <https://doi.org/10.1126/science.1109454>, 2005.

849 Tao, S., Eglinton, T. I., Montluçon, D. B., McIntyre, C., and Zhao, M.: Pre-aged soil organic carbon as a major
850 component of the Yellow River suspended load: Regional significance and global relevance, *Earth and Planetary
851 Science Letters*, 414, 77–86, <https://doi.org/10.1016/j.epsl.2015.01.004>, 2015.

852 Tao, S., Eglinton, T. I., Montluçon, D. B., McIntyre, C., and Zhao, M.: Diverse origins and pre-depositional histories
853 of organic matter in contemporary Chinese marginal sea sediments, *Geochimica et Cosmochimica Acta*, 191, 70–88,
854 <https://doi.org/10.1016/j.gca.2016.07.019>, 2016.

855 Tao, S., Eglinton, T. I., Zhang, L., Yi, Z., Montluçon, D. B., McIntyre, C., Yu, M., and Zhao, M.: Temporal variability
856 in composition and fluxes of Yellow River particulate organic matter, *Limnology and Oceanography*, 63, S119–S141,
857 <https://doi.org/10.1002/lno.10727>, 2018.

858 Turowski, J. M., Hilton, R. G., and Sparkes, R.: Decadal carbon discharge by a mountain stream is dominated by
859 coarse organic matter, *Geology*, 44, 27–30, 2016.

860 Walling, D. E. and Fang, D.: Recent trends in the suspended sediment loads of the world's rivers, *Global and Planetary
861 Change*, 39, 111–126, [https://doi.org/10.1016/S0921-8181\(03\)00020-1](https://doi.org/10.1016/S0921-8181(03)00020-1), 2003.

862 Wang, C., Li, F., Shi, H., Jin, Z., Sun, X., Zhang, F., Wu, F., and Kan, S.: The significant role of inorganic matters in
863 preservation and stability of soil organic carbon in the Baoji and Luochuan loess/paleosol profiles, Central China,
864 *CATENA*, 109, 186–194, <https://doi.org/10.1016/j.catena.2013.04.001>, 2013.

865 Wang, G., Feng, X., Han, J., Zhou, L., Tan, W., and Su, F.: Paleovegetation reconstruction using $\delta^{13}\text{C}$ of Soil Organic
866 Matter, *Biogeosciences*, 5, 1325–1337, <https://doi.org/10.5194/bg-5-1325-2008>, 2008.

867 Wang, H., Bi, N., Saito, Y., Wang, Y., Sun, X., Zhang, J., and Yang, Z.: Recent changes in sediment delivery by the
868 Huanghe (Yellow River) to the sea: Causes and environmental implications in its estuary, *Journal of Hydrology*, 391,
869 302–313, <https://doi.org/10.1016/j.jhydrol.2010.07.030>, 2010.

870 Wang, H., Wu, X., Bi, N., Li, S., Yuan, P., Wang, A., Syvitski, J. P. M., Saito, Y., Yang, Z., Liu, S., and Nittrouer, J.:
871 Impacts of the dam-orientated water-sediment regulation scheme on the lower reaches and delta of the Yellow River
872 (Huanghe): A review, *Global and Planetary Change*, 157, 93–113, <https://doi.org/10.1016/j.gloplacha.2017.08.005>,
873 2017.

874 Wang, H., Yang, Z., Saito, Y., Liu, J. P., Sun, X., and Wang, Y.: Stepwise decreases of the Huanghe (Yellow River)
875 sediment load (1950–2005): Impacts of climate change and human activities, *Global and Planetary Change*, 57, 331–
876 354, <https://doi.org/10.1016/j.gloplacha.2007.01.003>, 2007.

877 Wang, S., Fu, B., Piao, S., Lü, Y., Ciais, P., Feng, X., and Wang, Y.: Reduced sediment transport in the Yellow River
878 due to anthropogenic changes, *Nature Geosci*, 9, 38–41, <https://doi.org/10.1038/ngeo2602>, 2016.

879 Wang, X., Xu, C., Druffel, E. M., Xue, Y., and Qi, Y.: Two black carbon pools transported by the Changjiang and
880 Huanghe Rivers in China, *Global Biogeochemical Cycles*, 2016.

881 Weiguo, L., Xiahong, F., Youfeng, N., Qingle, Z., Yunning, C., and Zhisheng, A. N.: $\delta^{13}\text{C}$ variation of C3 and C4
882 plants across an Asian monsoon rainfall gradient in arid northwestern China, *Global Change Biology*, 11, 1094–1100,
883 <https://doi.org/10.1111/j.1365-2486.2005.00969.x>, 2005.

884 Xiubin, H., Tang, K., and Zhang, X.: Soil Erosion Dynamics on the Chinese Loess Plateau in the Last 10,000 Years,
885 *mred*, 24, 342–347, [https://doi.org/10.1659/0276-4741\(2004\)024\[0342:SEDOTC\]2.0.CO;2](https://doi.org/10.1659/0276-4741(2004)024[0342:SEDOTC]2.0.CO;2), 2004.

886 Xue, D., Lu, J., Leung, L. R., Teng, H., Song, F., Zhou, T., and Zhang, Y.: Robust projection of East Asian summer
887 monsoon rainfall based on dynamical modes of variability, *Nat Commun*, 14, 3856, [https://doi.org/10.1038/s41467-
888 023-39460-y](https://doi.org/10.1038/s41467-023-39460-y), 2023.

889 YRCC (Yellow River Conservation Committee): Annual Sediment Report for the Yellow River, 2016.

890 Yu, M., Eglinton, T. I., Haghypour, N., Montluçon, D. B., Wacker, L., Hou, P., Zhang, H., and Zhao, M.: Impacts of
891 Natural and Human-Induced Hydrological Variability on Particulate Organic Carbon Dynamics in the Yellow River,
892 *Environ Sci Technol*, 53, 1119–1129, <https://doi.org/10.1021/acs.est.8b04705>, 2019a.

893 Yu, M., Eglinton, T. I., Haghypour, N., Montluçon, D. B., Wacker, L., Wang, Z., Jin, G., and Zhao, M.: Molecular
894 isotopic insights into hydrodynamic controls on fluvial suspended particulate organic matter transport, *Geochimica et
895 Cosmochimica Acta*, 262, 78–91, <https://doi.org/10.1016/j.gca.2019.07.040>, 2019b.

896 Zhang, L. J., Wang, L., Cai, W. J., Liu, D. M., and Yu, Z. G.: Impact of human activities on organic carbon transport
897 in the Yellow River, *Biogeosciences*, 10, 2513–2524, <https://doi.org/10.5194/bg-10-2513-2013>, 2013.

898 Zhu, T. X.: Gully and tunnel erosion in the hilly Loess Plateau region, China, *Geomorphology*, 153–154, 144–155,
899 <https://doi.org/10.1016/j.geomorph.2012.02.019>, 2012.